Fault interaction and strain partitioning deduced from deformed fluvial terraces of the Eastern North Qilian foreland, NE Tibetan Plateau

Xiu HU[1], Yiran Wang[2], Wei-Tao Wang[3], Michael Oskin[2], Zhigang Zhi Li[4], Jinghao Lei[5], Youli Li[6], Peizhen Zhang[4], Wenjun Zheng[7], Kairong Lin[8], Shanfeng Xiao[9], Honghua Lu[10], Yi-Peng Zhang[11], Ruizhi Jin[12], Qingri Liu[5], and Yuezhi Zhong[13]

[1]Sun Yat-Sen university
[2]University of California, Davis
[3]School of earth science and geological engineering, Sun Yan-Sen University
[4]School of Earth Sciences and Engineering, Sun Yat-sen University
[5]Key Laboratory of Earth Surface Processes of Ministry of Education, Peking University, Beijing 100871, China
[6]Peking University
[7]Guangdong Provincial Key Laboratory of Geodynamics and Geohazards, School of Earth Sciences and Engineering, Sun Yat-Sen University
[8]Sun Yat-sen University
[9]Soochow University
[10]Key Laboratory of Geographic Information Science of Ministry of Education, School of Geographic Sciences, East China Normal University
[11]School of Earth Science and Geological Engineering, Sun Yat-Sen University
[12]Sun Yat-Sen University
[13]GFZ German Research Centre for Geosciences

March 05, 2024

Abstract

Faulting and folding of basement rocks together accommodate convergence within continental orogens, forming complex zones of intraplate deformation shaped by the fault interaction. Here we use the river terraces along the Dongda river to examine the tectonic deformation patterns of the hinterland and the foreland of the eastern North Qilian Shan, a zone of crustal shortening located at the northeast margin of the Tibetan Plateau. Five Late Pleistocene-Holocene terraces of Dongda river are displaced by three major reverse faults: Minle-Damaying fault, Huangcheng-Ta'erzhuang fault, and Fengle fault, from south to north. Based on displaced terrace treads, we estimated vertical slip rates along the Minle-Damaying fault as 0.7–1.2 mm/a, and along Fengle fault as 0.5–0.7 mm/a. Deformed terraces suggest additional uplift of ˜ 0.2 mm/a through folding of the Dahuang Shan anticline. Inhomogeneous uplift of the intermontane basins between the Minle-Damaying fault and the Dahuang Shan anticline indicates a 0.9 ± 0.2 mm/a uplift rate along the Huangcheng-Ta'erzhuang fault. Kinematic modeling of this thrust system shows that deformation propagated northward toward the foreland along a south-dipping 10° décollement rooted into Haiyuan fault at the depth of 20–25 km. This system accommodates 2.7–3.8 mm/a total crustal shortening rate. We suggest this broad thrust belt and the relatively high rate of shortening within this part of the eastern Qilian Shan is as a result of the oblique convergence along a restraining bend of Haiyuan fault system. The elevated shortening rate within this area indicates high

potential seismic hazard.

Hosted file

manuscript.docx available at https://authorea.com/users/745814/articles/717822-fault-interaction-and-strain-partitioning-deduced-from-deformed-fluvial-terraces-of-the-eastern-north-qilian-foreland-ne-tibetan-plateau

Hosted file

suppinfo.docx available at https://authorea.com/users/745814/articles/717822-fault-interaction-and-strain-partitioning-deduced-from-deformed-fluvial-terraces-of-the-eastern-north-qilian-foreland-ne-tibetan-plateau

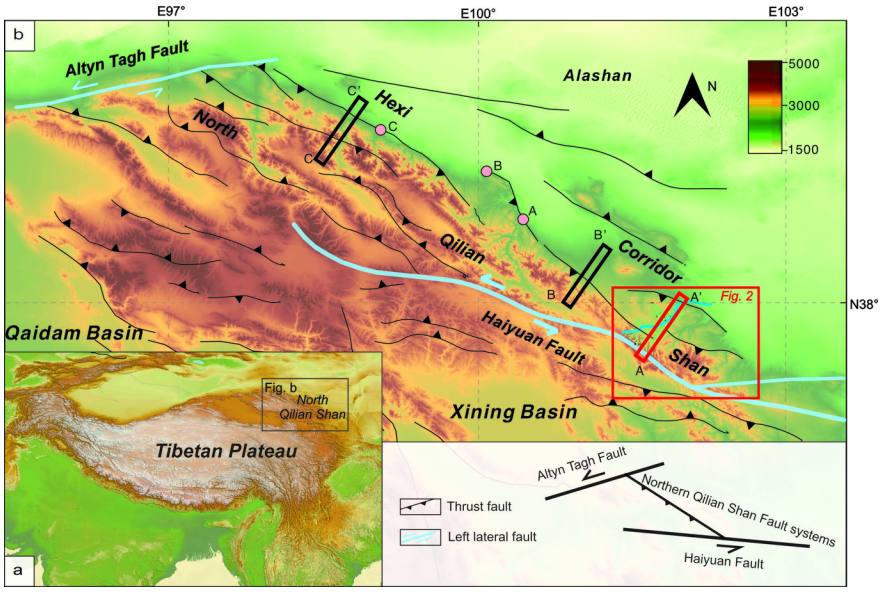

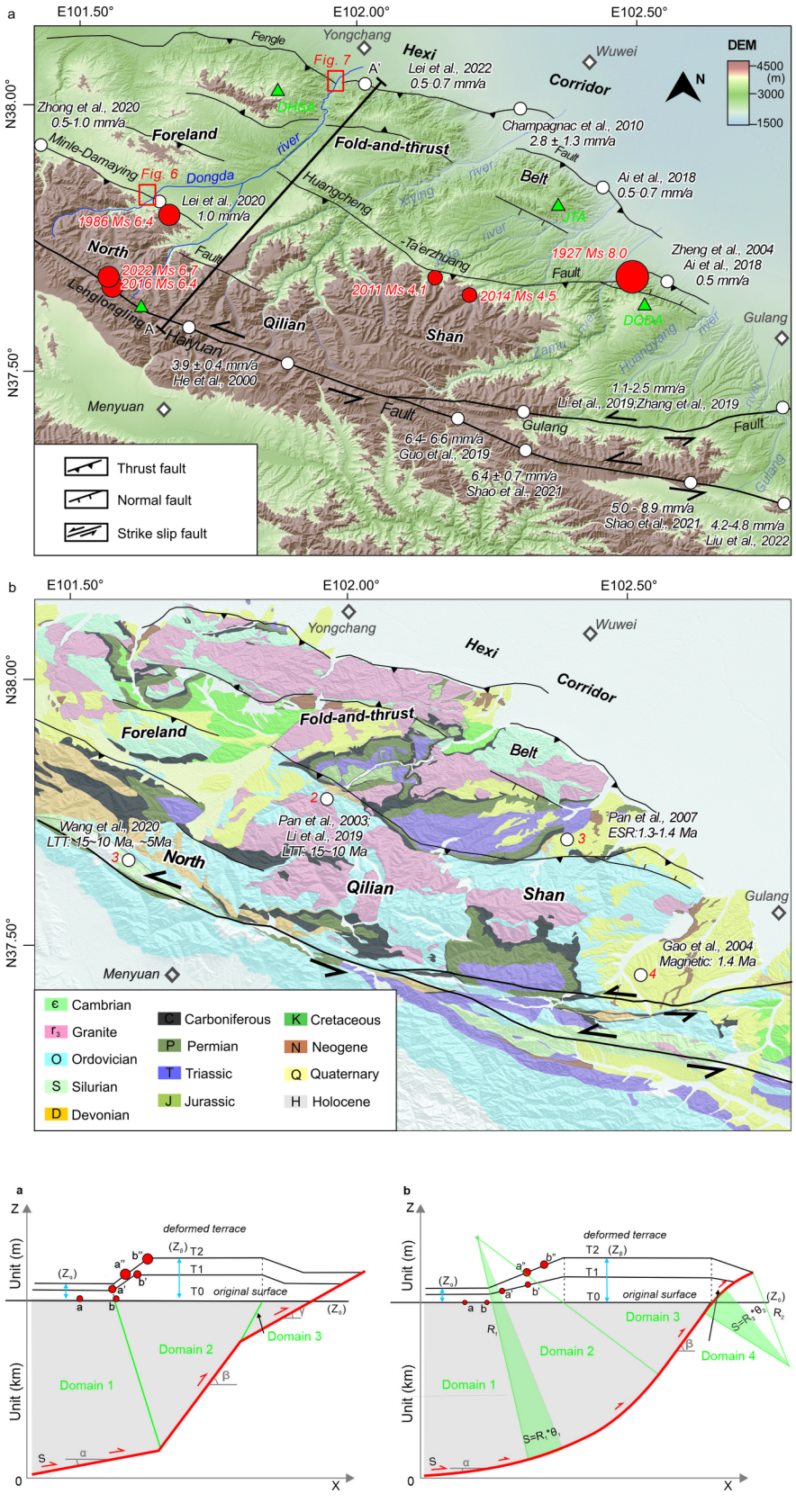

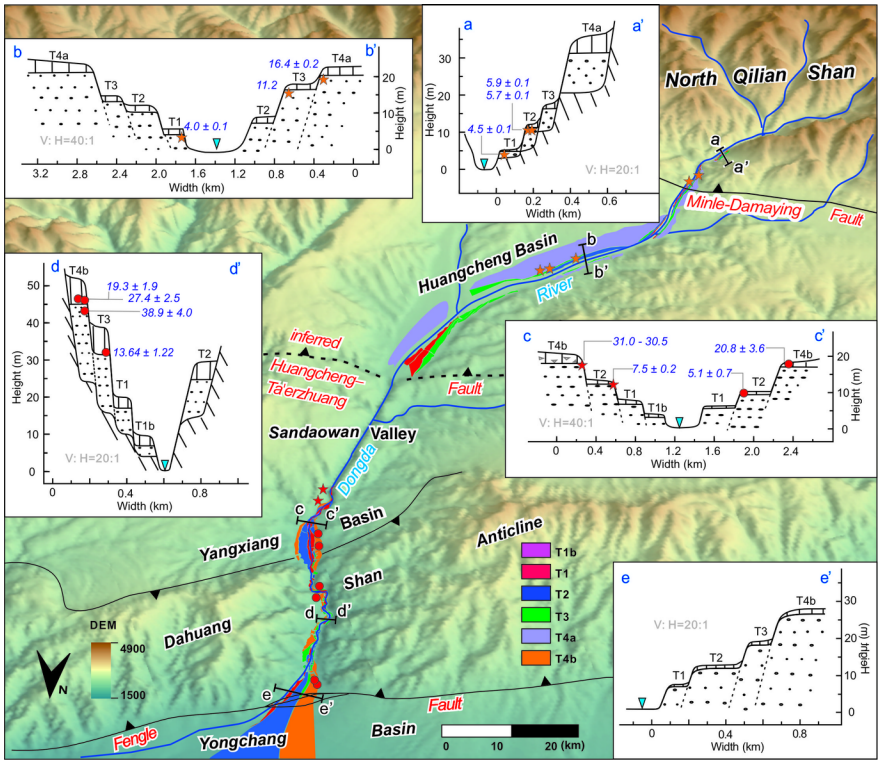

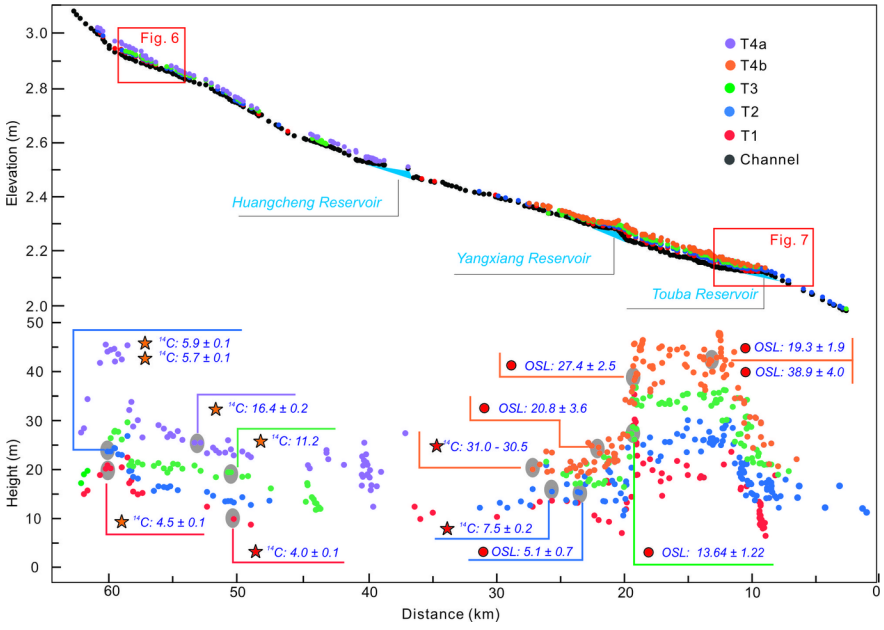

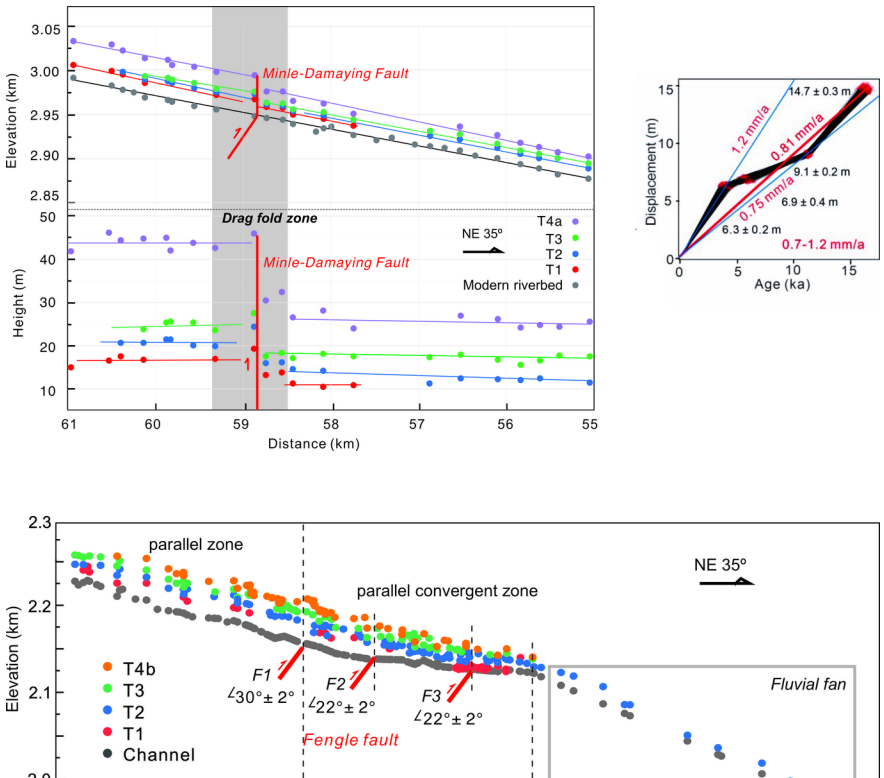

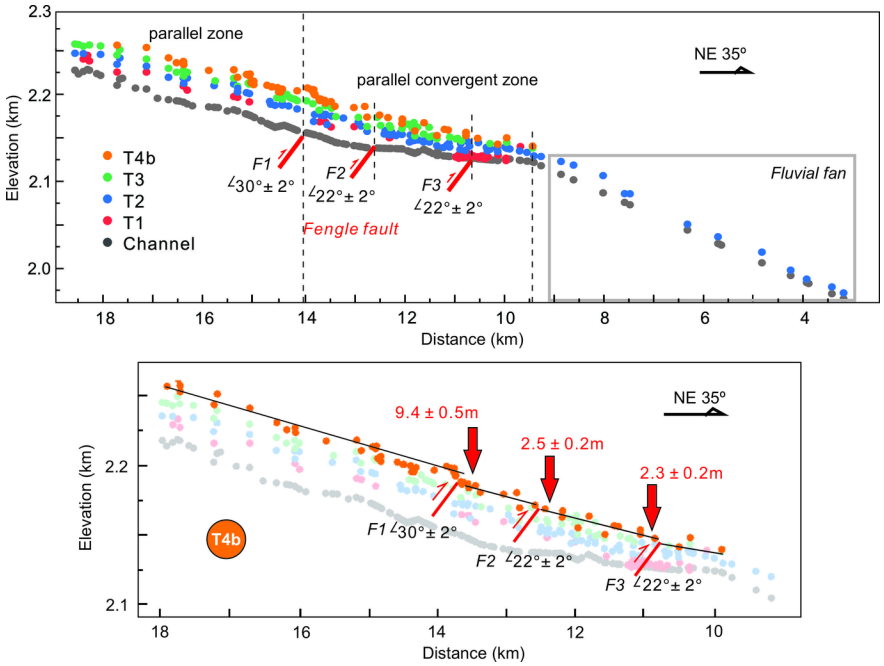

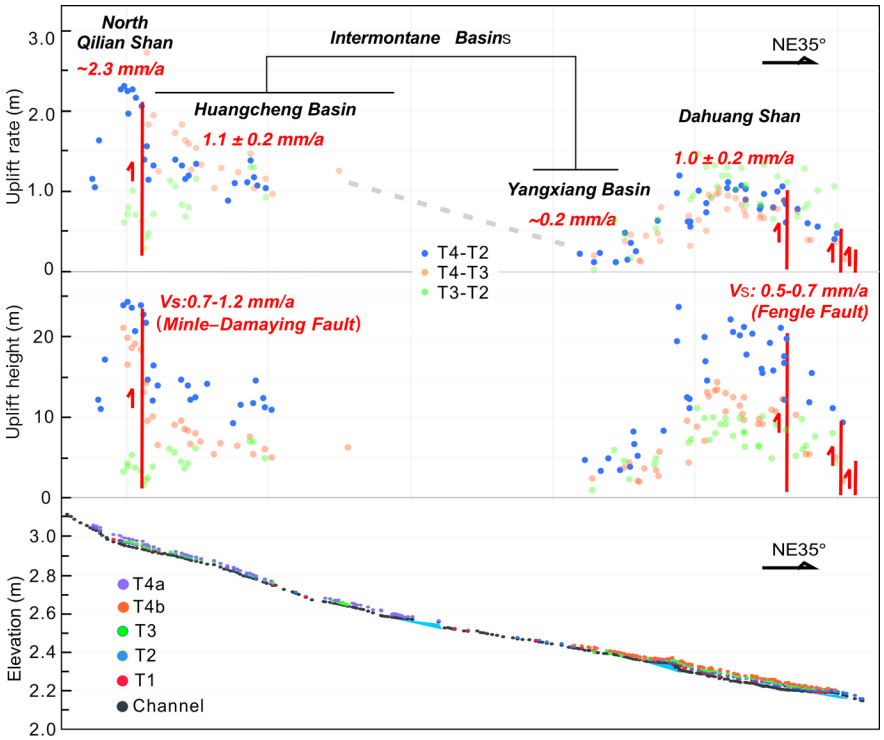

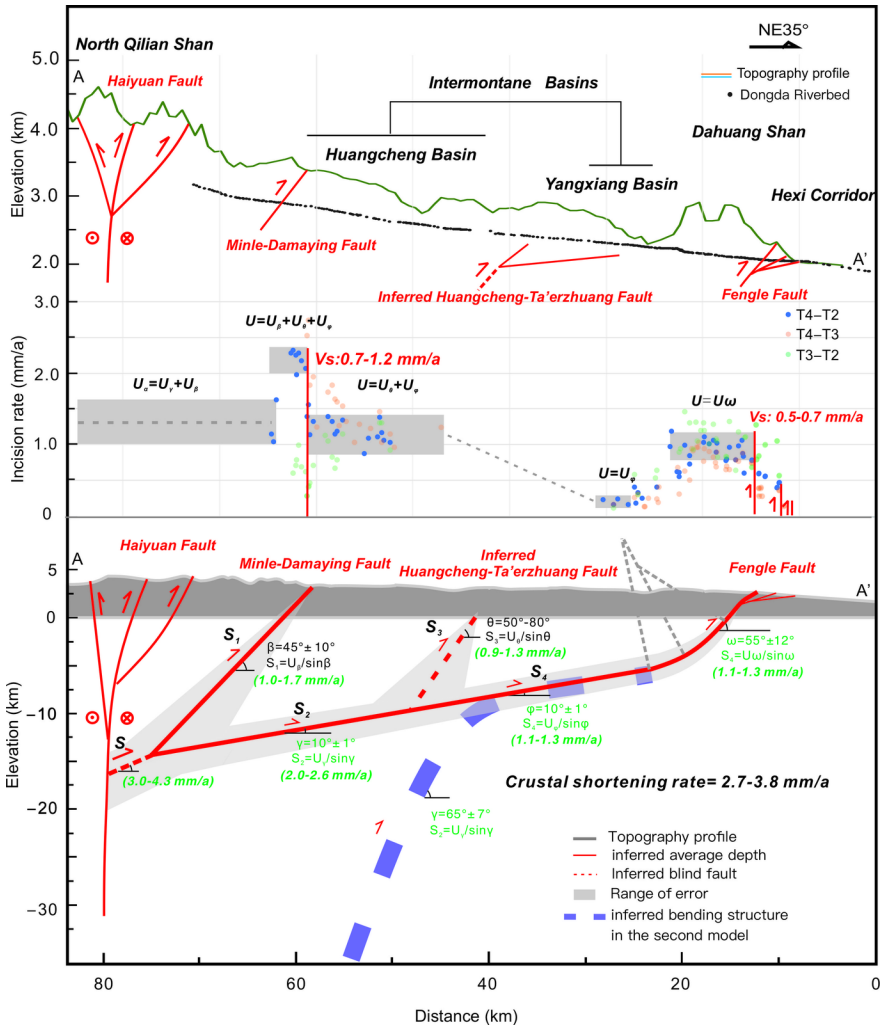

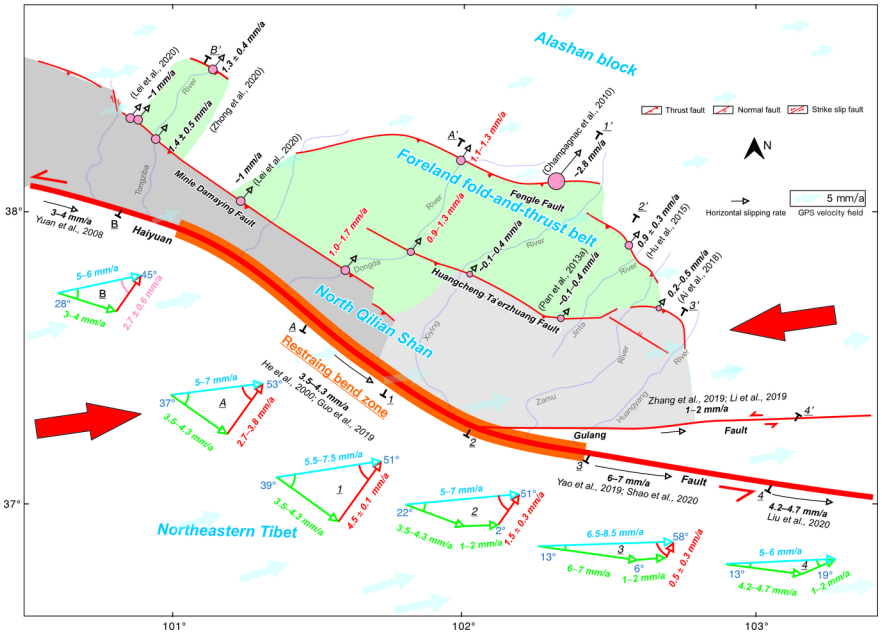

Fault interaction and strain partitioning deduced from deformed fluvial terraces of the Eastern North Qilian foreland, NE Tibetan Plateau

Xiu Hu[1, 3, 4, 5], Yiran Wang[2, 3, 4], Weitao Wang[1, 5], Michael E. Oskin[4], Zhigang Li[1, 5], Jinghao Lei[3, 4], Youli Li[3], Peizhen Zhang[1, 5], Wenjun Zheng[1, 5], Kairong Lin[6], Shanfeng Xiao[7], Honghua Lu[8], Yipeng Zhang[1], Ruizhi Jin[1], Qingri Liu[3], Yuezhi Zhong[3]

[1]School of Earth Sciences and Engineering, Guangdong provincial key laboratory of Geodynamics and Geohazards, Sun Yat-Sen University, Zhuhai, China
[2]Earth Observatory of Singapore, Nanyang Technological University, Singapore
[3]College of Urban and Environmental Sciences, Peking University, Beijing, China
[4]Department of Earth and Planetary Sciences, University of California, Davis, USA
[5]Southern Marine Science and Engineering Guangdong Laboratory, Zhuhai, China
[6]School of Civil Engineering, Sun Yat-Sen University, Zhuhai, China
[7]School of Mathematical Sciences, Soochow University, Suzhou, China
[8]Key Laboratory of Geographic Information Science of Ministry of Education, School of Geographic Sciences, East China Normal University, Shanghai, China

Corresponding author: Yiran Wang (yiranwangyr@gmail.com); Weitao Wang (wangweitao@mail.sysu.edu.cn)

Key Points:

- Eastern North Qilian is formed as a belt of northward-verging thrust faults above a ~10° décollement layer rooted into Haiyuan fault.
- The activity of the three active thrust systems within this 70 km-wide belt accommodates 2.7–3.8 mm/a of crustal shortening.
- The high shortening rate here is the result of localized convergence within a restraining bend of the Haiyuan fault.

Abstract

Faulting and folding of basement rocks together accommodate convergence within continental orogens, forming complex zones of intraplate deformation shaped by the fault interaction. Here we use the river terraces along the Dongda river to examine the tectonic deformation patterns of the hinterland and the foreland of the eastern North Qilian Shan, a zone of crustal shortening located at the northeast margin of the Tibetan Plateau. Five Late Pleistocene-Holocene terraces of Dongda river are displaced by three major reverse faults: Minle-Damaying fault, Huangcheng-Ta'erzhuang fault, and Fengle fault, from south to north. Based on displaced terrace treads, we estimated vertical slip rates along the Minle-Damaying fault as 0.7–1.2 mm/a, and along Fengle fault as 0.5–0.7 mm/a. Deformed terraces suggest additional uplift of ~ 0.2 mm/a through folding of the Dahuang Shan anticline. Inhomogeneous uplift of the intermontane basins between the Minle-Damaying fault and the Dahuang Shan anticline indicates a 0.9 ± 0.2 mm/a uplift rate along the Huangcheng-Ta'erzhuang fault. Kinematic modeling of this thrust system shows that deformation propagated northward toward the foreland along a south-dipping 10° décollement rooted into Haiyuan fault at the depth of 20–25 km. This system accommodates 2.7–3.8 mm/a total crustal shortening rate. We suggest this broad thrust belt and the relatively high rate of shortening within this part of the eastern Qilian Shan is as a result of the oblique convergence along a restraining bend of Haiyuan fault system. The elevated shortening rate within this area indicates high potential seismic hazard.

Plain Language Summary

The eastern North Qilian Shan and its foreland basin exhibit a complex structure and spatially varying shortening rate because the area is not only deformed by the North Qilian frontal thrust system, but also under the influence of the adjacent Haiyuan strike-slip fault. A restraining bend along Haiyuan fault leads to additional compressional strain concentrated in this area, which results in the development of a widely uplifted and deformed region to the north, within the Qilian Shan mountains. Through geomorphic survey of the riverbed and terrace elevations of the Dongda river, we find the most uplift is concentrated along the northernmost, lowest range adjacent to the foreland basin (~0.6 mm/a) and at the North Qilian mountain front bounding the higher peaks (~1 mm/a). We suggest that this wide zone of active faulting formed along multiple strands of high angle reverse faults that sole into a single deep detachment, and this structure has accommodated one of the highest rates of crustal shortening (over 3 mm/a) documented within the North Qilian. This results in an elevated seismic hazard in the nearby populated foreland basin.

1 Introduction

Foreland fold-and-thrust belts form as the compressional orogen evolves and the deformation front propagates into the foreland basin. Within an intraplate convergence zone, shortening may involve multiple pairs of fold and thrust, and each pair may have distinct history of tectonic activity (McQuarrie et al., 2005; Cooke and Dair, 2011; Horton et al., 2022; Moulin and Cowgill, 2023). As a fold-and-thrust belt evolves, the tectonic activity and the deformation pattern may change over time (Lu et al., 2019; Sun et al., 2022; Zhang et al., 2023; Wang et al., 2024). Youthful deformed markers, such as river terraces or uplifted relict geomorphic surfaces, may be used to deduce tectonic activity of single faults (Lavé and Avouac, 2000; Burbank and Anderson, 2012; Yang and Li, 2017; Wang et al., 2020), and, if of sufficient extent, can reveal the tectonic relationship between structures (Hoke et al., 2014; Zhong et al., 2020). By converting surface

deformation that varies with space and time into geological cross section, it is possible to unravel the geometries and kinematics of a fold-and-thrust belt to better understand the evolution of its constituent thrust faults (Burbank et al., 1996; Tapponnier et al., 1990; 2001; Ori and Friend, 1984; Siks and Horton, 2011; Yonkee et al., 2019).

As the northeastern margin of the Tibetan plateau, the eastern North Qilian Shan shows complex deformation history involving interactions between multiple fault systems. Here, oblique convergence has been accommodated both by compression along reverse faults and left slip on sinistral faults since the inception of uplift ca. 15–10 Ma ago (Meyer et al., 1998; Zheng et al., 2013; Allen et al., 2017; Zuza et al., 2016, 2018) (Figure 1). Bounded by the Haiyuan fault to the south and the Fengle fault to the north, a 70 km-wide foreland fold-and-thrust belt has developed within the eastern North Qilian Shan adjacent the restraining bend of the Haiyuan fault (Figures 1 and 2) (Gaudemer et al., 1995). Previous geomorphology studies show that this fold-and-thrust belt involves activity of multiple strands of faults (Tapponnier et al., 1990; Li and Yang, 1998; Hu et al., 2015; Ai et al., 2017; Lei et al., 2020). However, most studies were only focused on a single structure, while the growth and interaction of the set of structures, how the multiple active structures recognized here work together to accommodate crustal shortening, and the relationship of this fold and thrust belt to the kinematics of the Haiyuan fault restraining bend are not fully understood.

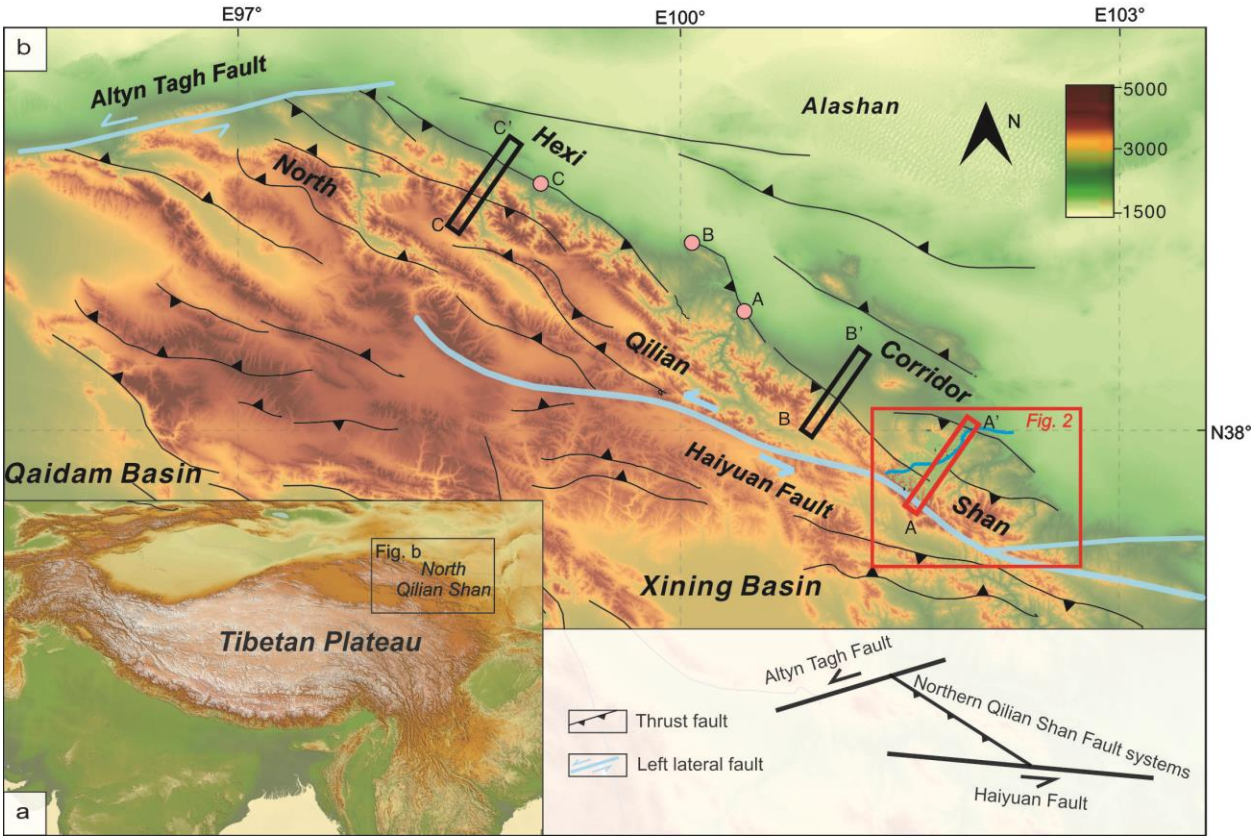

Figure 1 a. The Tibetan plateau block and the location of North Qilian Shan **b.** Map of North Qilian Shan active fault system and the location of our study area. Pink circles show the locations for the slip rates studies of individual active faults (A: eastern Yumushan fault, Hu et al., 2019; B: North Yumushan fault, Tapponnier et al., 1990; C: Fodongmiao-Hongyazi fault,

Hetzel et al., 2019), and grey stripes show the locations for integrated cross-section analysis and slip rates studies across the frontal thrust systems (A-A': this study; B-B': Tongziba river, Zhong et al., 2020; C-C': Beida river, Wang et al., 2020).

In this study, we document the activity of the eastern North Qilian Shan from folding and faulting of river terraces of the Dongda river. A sequence of river terraces record deformation across the entire fold-and-thrust belt, revealing how thrusting partitions between different structures. Through integrating tectonic geomorphology and Quaternary geochronology, we describe the uplift rate distribution along the Dongda River. Through kinematic modeling, we develop a structural model to explain surface deformation across the thrust belt. Through comparing the shortening rate along the Dongda River with surrounding areas, we summarize the deformation pattern along the eastern North Qilian Shan fold-and-thrust belt.

2 Geological Setting

The eastern North Qilian Shan in our research area reaches an elevation of 5217 m and is characterized by steep hillslopes and deep valleys. Over the Cenozoic, significant exhumation, revealed via low temperature thermochronology, suggests that the present topography of the North Qilian Shan was developed mostly since the Miocene (Pan et al., 2013b; Li et al., 2019; Wang et al., 2020) (Figure 2a). As the thrust belt propagated toward the foreland, reverse faulting has led to development of a series of Cenozoic intermontane basins and low hills, forming a ~70 km wide foreland fold-and-thrust belt (Figure 2b). Previous studies suggest that the foreland fold-and-thrust belt was developed due to deformation surrounding a restraining bend of the Haiyuan Fault (Gaudemer et al., 1995; Li et al., 2019). A series of earthquakes with magnitude greater than M4.0 have taken place around the region since 1920 AD (Figure 2a) (Deng, 2007). The restraining section of the Haiyuan fault, known as the Lenglongling segment, is characterized by a major left-lateral strike-slip component and a minor dip-slip component within the upper Dongda River basin. The Haiyuan fault has a Quaternary lateral slip rate of 3.5–6.9 mm/a (Gaudemer et al., 1995; He et al., 2000; Guo et al., 2019; Yao et al., 2019; Shao et al., 2020; Liu et al., 2022), and has been identified as source of the 2016 *Ms*6.4 and 2022 *Mw6.7* Menyuan earthquake, as well as the 1920 *Ms8.0* Haiyuan earthquake east of our study area (Guo et al., 2017; Luo and Wang, 2022; Niu et al., 2023). The Gulang fault (Figure 2) branches off from the Haiyuan fault, with a lateral slip rate of 1–2 mm/a (Zhang et al., 2019; Li et al., 2019). This fault, or one of the faults within the adjacent fold and thrust belt, may have been the source for the 1927 *Ms*8.0 Gulang earthquake (Gaudemer et al., 1995; Guo et al., 2020).

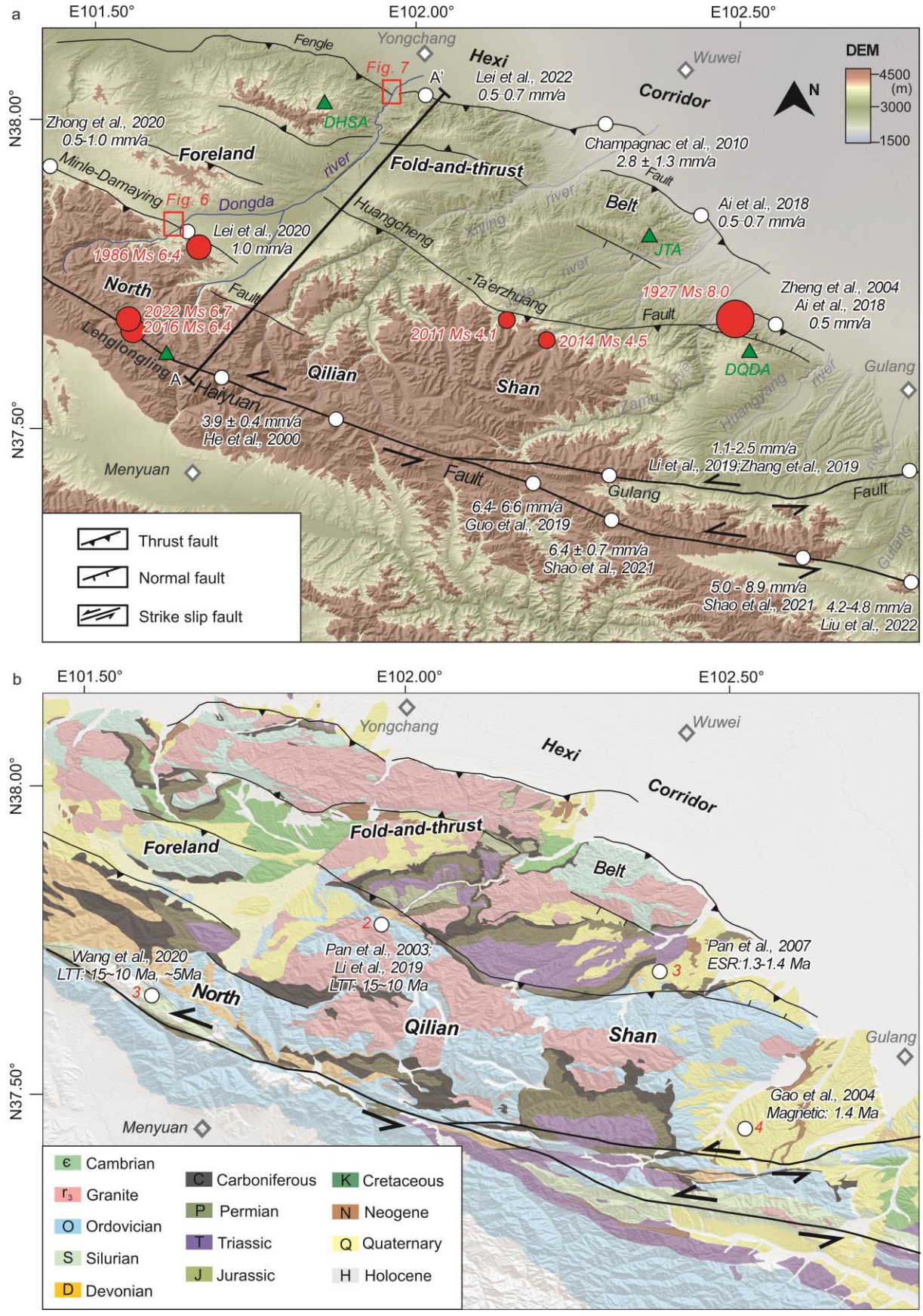
a
E101.50°
E102.00°
E102.50°
N38.00°
N37.50°
Fengle
Yongchang
Hexi
Corridor
Wuwei
Fig. 7
A'
A
DHSA
Lei et al., 2022
0.5-0.7 mm/a
DEM
4500
(m)
3000
1500
N
Zhong et al., 2020
0.5-1.0 mm/a
Foreland
Minle-Damaying
Fig. 6
Dongda
river
Fold-and-thrust
Huangcheng
Champagnac et al., 2010
2.8 ± 1.3 mm/a
Fault
Belt
Ai et al., 2018
0.5-0.7 mm/a
Lei et al., 2020
1.0 mm/a
1986 Ms 6.4
North
Fault
2022 Ms 6.7
2016 Ms 6.4
Lenglongling
JTA
Ta'erzhuang
1927 Ms 8.0
Zheng et al., 2004
Ai et al., 2018
0.5 mm/a
2011 Ms 4.1
2014 Ms 4.5
DQDA
Qilian
Shan
Gulang
Huangyang
Zamu
Haiyuan
3.9 ± 0.4 mm/a
He et al., 2000
Menyuan
1.1-2.5 mm/a
Li et al., 2019;Zhang et al., 2019
Fault
Gulang
6.4- 6.6 mm/a
Guo et al., 2019
6.4 ± 0.7 mm/a
Shao et al., 2021
5.0 - 8.9 mm/a
Shao et al., 2021
4.2-4.8 mm/a
Liu et al., 2022
Thrust fault
Normal fault
Strike slip fault
b
E101.50°
E102.00°
E102.50°
N38.00°
N37.50°
Yongchang
Wuwei
Hexi
Corridor
Foreland
Fold-and-thrust
Belt
2
Pan et al., 2003;
Li et al., 2019
LTT: 15~10 Ma
Wang et al., 2020
LTT: ~15~10 Ma, ~5Ma
3
Pan et al., 2007
ESR:1.3-1.4 Ma
North
Qilian
Shan
Gulang
Gao et al., 2004
Magnetic: 1.4 Ma
4
Menyuan
Cambrian
Granite
Ordovician
Silurian
Devonian
Carboniferous
Permian
Triassic
Jurassic
Cretaceous
Neogene
Quaternary
Holocene

125

Figure 2 a. The active fault systems and the river systems of the area. The white circle with black characters shows the study sites for Quaternary thrust vertical slip rates and left lateral slip rates. The green triangle signs the locations for the specific fold segments. DQDA: Dongqingding anticline, JTA: Jinta anticline, DHSA: Dahuang Shan anticline. **b**. General geologic setting of the eastern Qilian Shan. The white circle shows the study site for Low Temperature Thermochronology (LTT), and the loess-and-paleosol sequences (ESR and Magnetic).

Several major rivers, Dongda, Xiying, Jinta, Zamu, and Huangyang River, originate from the eastern North Qilian Shan and drain northeastward through the foreland fold-and-thrust belt into the Hexi Corridor. These rivers cross three major reverse faults within the North Qilian Shan mountain front and foreland basin: Minle-Damaying fault, Huangcheng-Ta'erzhuang fault, and Fengle fault (Figure 2a). Fluvial terraces of the major rivers, often covered by thick layers of loess, have all been deformed by these faults, and have been the focus of active fault study in this area (e.g. Pan et al., 2013a; Hu et al., 2015). The southernmost fault, the Minle-Damaying fault is the frontal fault of the Minle basin which is west of our study area, and was the seismogenic fault of the 1986 *Ms 6.4* earthquake (He et al., 2020). Offset terraces of the Tongziba river and Xie river support an uplift rate of 0.5–1.0 mm/a across this fault with a dip angle between 30–45° at surface (Xiong et al., 2017; Lei et al., 2020; Zhong et al., 2020). 20 km north of the Minle-Damaying fault, Huangcheng-Ta'erzhuang fault ruptured the late Pleistocene alluvial fan surfaces at the Dongqingding point, with a vertical slip rate of 0.5 mm/a (Hou, 1998; Zheng et al., 2004; Ai et al., 2017), and it is identified as the seismogenic fault for the 2011 *Ms*4.1 and 2014 *Ms*4.5 earthquakes. The vertical uplift rate of the northernmost Fengle fault varies from 0.5–0.7 mm/a (Lei et al., 2021), to 2.8 ± 1.3 mm/a (Champagnac et al., 2010), then to 0.5–0.7 mm/a (Ai et al., 2017) from west to east based on displaced alluvial fans. Slip on the Fengle fault is associated with folding of the Dahuang Shan anticline in the Dongda river area (Gaudemer et al., 1995; Hu et al., 2015). To the south, the fold backlimb is bounded by a north-dipping back thrust (Gaudemer et al., 1995).

Pre-Cambrian to Cretaceous basement rocks are widely exposed within the eastern North Qilian Shan and the adjacent fold-and-thrust belt (Gansu Bureau of Geology and Mineral Resources, 1989) (Figure 2b). In our research area, along the Dongda River, Cambrian to Silurian rocks, the basement of this region, are deformed, metamorphosed and intruded by Caledonian age granodiorites and granite (Li et al., 2019). The highly deformed Devonian Laojun Shan group, a typical continental molasse deposit consisting of sandstone with mudstone, is widely distributed within the North Qilian Shan and separated from the crystalline basement by an unconformity (Gansu Bureau of Geology and Mineral Resources, 1989) (Figure 2b). Above these deposits are Carboniferous black shale with interbeds of fossiliferous marine limestone, covered by a sequence of Permian-Triassic continental sandstone and conglomerates. These rocks are mainly exposed at the hangingwall of Minle-Damaying fault and between the Huangcheng-Ta'erzhuang fault and the Dahuang Shan anticline. This sequence implies a transformation from shallow marine to continental clastic sedimentation (Gaudemer et al., 1995). A set of Cretaceous sandstone and conglomerates are exposed between the Huangcheng-Ta'erzhuang fault and the back thrust of Dahuang Shan anticline, implying the deposition within the pull-apart basin or synclinal trough at that time (Gaudemer et al., 1995). Between the Haiyuan Fault and Minle-Damaying Fault, no Mesozoic and Cenozoic strata are preserved. In the footwall of the Minle-Damaying Fault, an unconformity between Cretaceous and Neogene-Quaternary deposits suggests that there was a major sedimentary hiatus during the Paleogene. Reddish Neogene

sandstones and siltstones, at least 500 m thick, distributed between the Huangcheng-Ta'erzhuang fault and the Dahuang Shan anticline, reflect deposition within a foreland basin during an earlier phase of uplift of the North Qilian Shan. Over the Pleistocene, folding and thrusting has propagated to the north of the Minle-Damaying fault to the Fengle fault. This region was also blanketed with loess up to hundreds of meters thick as it was uplifted. Geochronology studies of deformed terrace deposits beneath the oldest loess deposits suggest that uplift was underway by 1.3–1.4 Ma (Gaudemer et al., 1995; Pan et al., 2007).

3 Method

3.1 Fieldwork

Aided by analysis of Google Earth imagery and a 90 m resolution digital elevation model (DEM) from the Shuttle Radar Topography Mission (Farr et al., 2007), we mapped the Dongda river terrace surfaces in the field (Figure S1). Terrace elevations (Table S1) were measured using a hand-held differential Global Positioning System (GPS) with 2 to 5 cm horizontal and vertical precision and the Truepulse200x laser rangefinder with 4 cm horizontal errors for targets within 400 m distance, 15 cm horizontal errors for targets between 400-1000 m, and 0.1° degree of inclination accuracy. Stratigraphy of terrace deposits were described based on natural outcrops, including contacts, bedding thickness, bed geometry, grain size and internal sedimentary structures. We then reconstructed the sedimentary facies and depositional architecture and establish terrace cross sections (Figure 4).

3.2 Geochronology

We estimated terrace abandonment ages by dating the bottom of aeolian loess cover, as it has been proved in this area that loess accumulation started right after the abandonment of terrace treads since early Pleistocene (Gao et al., 2004). We also collected samples from sand interbeds within the fluvial gravels, which we use to constrain the maximum age of terrace abandonment. In this work, we report six new optical stimulated luminescence (OSL) and three ^{14}C dates, and we incorporated the earlier dating results reported by Xiong et al. (2017) and Lei et al. (2020) to further bracket the age of the terraces. The results are reported in Tables 1 and 2.

3.2.1 ^{14}C-dating

Charcoal for ^{14}C-dating was collected from loess or colluvium deposits overlying each terrace tread (Figure S2). As these charcoal samples are post-fire remains, in situ or detrital, the age should be similar or older than the overlying sediments. These charcoal samples were analyzed at the School of Archaeology and Museology, Peking University. In the laboratory, each sample was pretreated using the acid-alkali-acid (AAA) sequence to remove contaminants (Vries and Barendsen, 1954) and was then transformed into graphite under standard procedures. Accelerator Mass Spectrometry (AMS) was employed to measure ^{14}C concentration in samples of these materials relative to modern standards based on the approach of Talma and Vogel. (1993). All sample ages were determined with Libby's half-life (5,568 years), and the results were calibrated by IntCal20 atmospheric curve (Reimer et al., 2020) in the software OxCal v4.4 (Ramsey, 2009). Dates are reported as years before present (present = AD 1950).

3.2.2 OSL dating

Late Pleistocene aeolian loess provides reliable OSL dates because long-duration exposure to sunlight prior to deposition ensures complete bleaching (Aitken, 1998). Five samples were taken from the bottom of capping loess deposits, constraining the minimum age of abandonment of the paleo-riverbed, and one sample were taken from the fine sand layers from the upper section of the gravel layers, constraining the maximum abandonment age of the paleo-riverbed (Figure S2). All these samples were collected by hammering 25 cm long stainless steel cubes into loess or sand layers that were buried at least 30 cm deep. Sample tubes remained sealed with opaque materials until processed in the lab. Sample measurements were conducted in the OSL Chronology Laboratory of the Institute of Crustal Dynamics, China Earthquake Administration. In the lab, the polymineralic fine-grained (4~11 μm) minerals were extracted and pretreated for equivalent dose determination. Equivalent dose (De) measurement was determined using the Simplified Multiple Aliquot Regenerative-dose (SMAR) procedure, and the environmental dose rate (D), U, Th, and K contents in the samples were measured using Canberra GC4018 (Aitken, 1998). All these samples show no obvious saturated trend for De. Thus, OSL date for the measured sample was calculated from ratio of the acquired De to environmental dose rate, D.

3.3 Fault structure analysis

To interpret the tectonic signal and deduce underlying structure from the terrace surfaces, we correlate the terrace surfaces using both the absolute elevations and the relative heights above the present channel perpendicular to thrust-fault strike (Figures 5, 6, 7). The tectonic uplift from the North Qilian mountain front to its fold-and-thrust belt in Hexi Corridor were interpreted using the relative incision rates calculated for different terrace levels (Figure 8). These interpretations of surface tectonic deformation are combined with the regional topography, fault displacement from field survey, and knowledge of fault orientation and fault activity from previous research to construct a schematic regional cross section (Figure 9) and to constrain the overall structure and estimate the cumulative shortening.

3.3.1 Fault scarp offsets

To measure tectonic deformation (throw) across individual faults, we projected the terrace longitudinal profile to a vertical plane (striking NE35°) perpendicular to the strike of the North Qilian thrusts. Where drag folding has formed near the fault plane, or when faulting is distributed across several strands we project terrace surfaces from outside of the deformation zone to constrain fault throw (Figure 6). For faults with several fault branches, we also measure offset from scarp height on individual strands (Figure 7). Fault throw measurements are combined with the fault dip measured from outcrops or palaeoseismic trenches, to infer shortening and displacement rate for each fault.

3.3.2 Fault-related-fold model

To deduce the geometry and kinematics of the active structures of eastern North Qilian Shan, we modeled the shape of deformed river terraces with various fault geometries. We consider two end-member models for folding over a fault: fault-bend folding produced by a discrete change in fault dip (Suppe, 1983) (Figure 3a), and tilting over a listric bend (Erslev et al., 1986) (Figure 3b). The model built is based on kinematics solutions for the slip embedded in different domains, and then tracked the marker terrace surfaces on the cross section to generate the estimates for

surface deformation (Amos et al., 2007; Chen et al., 2007; Hu et al., 2015). A best-fit model for underlying fault location, geometry and kinematics was developed through comparing these uplift estimates to terrace deformation.

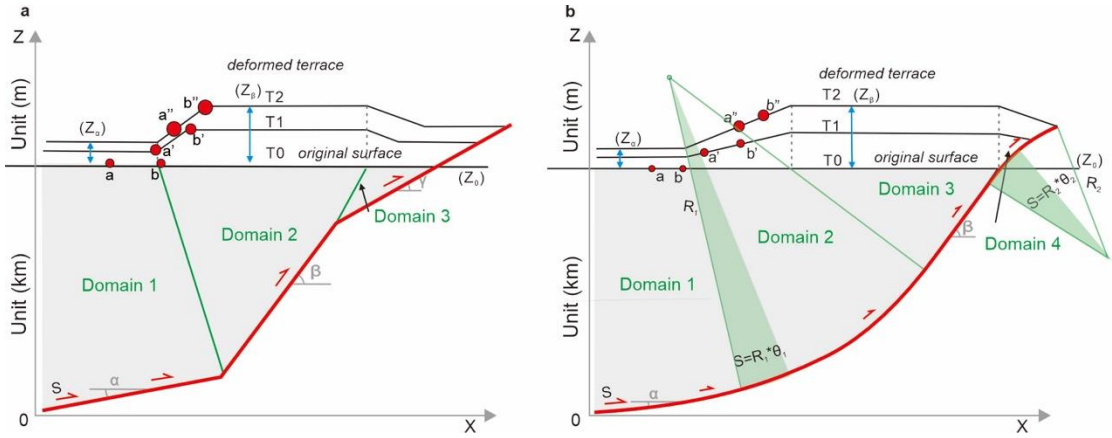

Figure 3 a, b Comparison of deformation over a fault-bend fold versus a listric fault. The length and progressive tilting of the fold backlimb may be used to determining the correct model.

To constraint the relative uplift within the planar fault segments, we assume that slip rate (S) remains approximately constant along every segment of the fault plane. When the fault changes its dip angle from α, to β, and , the tectonic uplift rate at the corresponding domains associated with fold growth over time t may be expressed as follows.

$$\frac{Z_\alpha - Z_0}{\sin\alpha} = \frac{Z_\beta - Z_0}{\sin\beta} = S * t$$

where Z_α, Z_β respond to the elevation of different terrace segments above the paleo-river elevation, Z_0. This equation may be simplified as

$$\frac{Z_\alpha - Z_\beta}{\sin\alpha - \sin\beta} = S * t \quad (1)$$ (Thompson et al., 2002)

For the planar fault-bend fold, we expect flights of terraces parallel to each other (Figure 3a). When terraces deformed above a fault bend (dip angle α to β), we trace the points a, b across the planar bend, the slope of deformed points a', b' at T1 (with distance and elevation of $X_{a'}$, $X_{b'}$; and $Z_{a'}, Z_{b'}$, respectively) and that of a'', b'' at T2 (with distance and elevation of $X_{a''}$, $X_{b''}$; and $Z_{a''}, Z_{b''}$, respectively) would be expressed as function (2), illustrating that slope of the relative terrace profile keeps constant, which can be calculated from the change of the fault dip

$$\text{slope} = \frac{Z_{b'} - Z_{a'}}{X_{b'} - X_{a'}} = \frac{Z_{b''} - Z_{a''}}{X_{b''} - X_{a''}} = \frac{\sin\beta - \sin\alpha}{\cos\beta} \quad (2)$$ (Figure 3b)

For the listric model, we divide the deformed terrace tread geometry into divergent and convergent zones where terrace tread dip increases with age. Over a convex listric fault, the upward rotation of the terrace surfaces increases with terrace age, forming a divergent zone. Like the planar fault, we trace the points a, b across the listric bend, the slopes between points a', b' at T1 (with distance and elevation of $X_{a'}$, $X_{b'}$; and $Z_{a'}, Z_{b'}$, respectively), and that of points a'', b'' at T2 (with distance and elevation of $X_{a''}$, $X_{b''}$; and $Z_{a''}, Z_{b''}$, respectively) would express as function (3). For a concave, or antilistric fault, the downward rotation of the terrace surfaces also increases with terrace age, but in an opposite sense, forming the convergent zone. Above a listric segment, we assume a cylindrical fault with single radius of curvature, R. For the slip rate

$S = R * \theta$ (Figure 3b), we divide the curvature into units of arcs of θ. After a given time t, the gradient of deformed terrace can be expressed as (3)

$$\text{slope} = \frac{Z_{b'} - Z_{a'}}{X_{b'} - X_{a'}} = \frac{Z_{b''} - Z_{a''}}{X_{b''} - X_{a''}} = \tan(t\theta) \quad (3)$$ (Figure 3b)

We employed Origin Lab and MATLAB software, to compute the terraces height and gradient relative to the riverbed with uncertainties. We simulated the vertical slip rate by sampling errors from linear fits to terrace tread profiles, abandonment ages, and fault dips from their respective frequency distributions. We approach these interrelated uncertainties with Monte Carlo simulation, over 10^3 trials to constraint the results with 95% confidence. Based on the interpreted surface deformation data, we conduct the MATLAB simulation to estimate the geometry and slip behavior of underlying faults, the dip angle, and accumulated depth with uncertainties are explored with constraints from surface observations of fault location and dip.

4 Results

4.1 Terrace sequences and structures

Flights of fluvial terraces are well developed and preserved along the Dongda river (Figure S1). We divide the Dongda River into six segments from south to north: North Qilian Shan, Huangcheng basin, Sandaowan valley, Yangxiang basin, Dahuang Shan anticline and Yongchang basin (Figure 4).

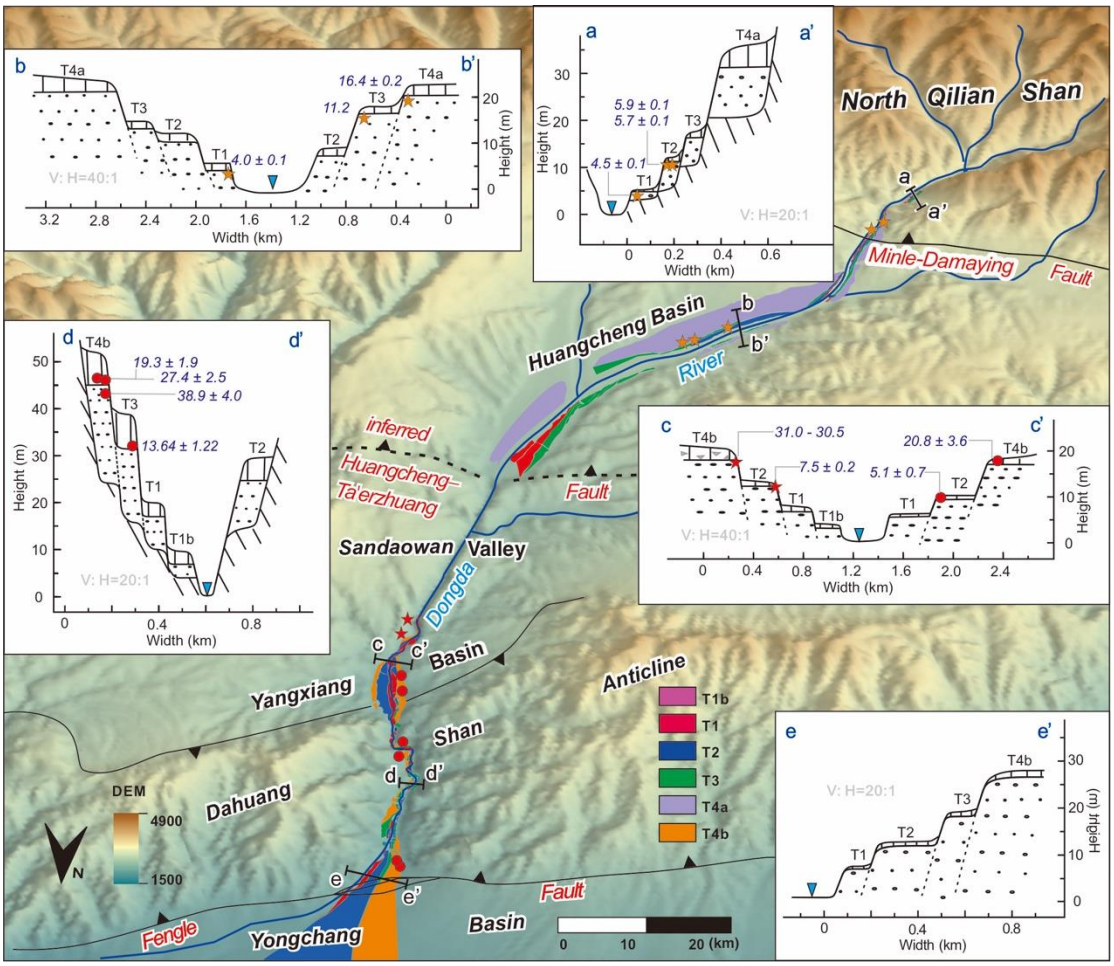

Figure 4 Elevation map the Dongda River zone, and the schematic cross-sections of terrace stratigraphy, keyed to numbered locations in the elevation map. The basin is divided into North Qilian Shan, Huangcheng basin, Sandaowan valley, Yangxiang basin, Dahuang Shan anticline and Yongchang basin. Note that this map is oriented south side up. The orange stars indicate location of ages from Xiong et al. (2017) and Lei et al. (2020), and the red stars and the circles indicate the locations for the charcoal samples and the OSL samples, respectively, in this work.

There are four continuous terrace levels preserved along the Dongda River within the North Qilian Shan segment (T4a, T3, T2 and T1) (Figures 4, S1). The highest, T4a, is a fill terrace with tread elevations between 25 to 46 m above the riverbed and fluvial fill 9–12 m thick. The aeolian loess covering the T4a tread has a thickness between 6 m and 10 m. T3 and T2, have thinner, 5–8 m thick, gravel fills, with treads 17–30 m, and 12–22 m above riverbed, respectively. T1 is a strath terraces of which the bedrock strath is covered by a thin (2–4 m) gravel layer of rounded cobbles and boulders. Loess layers covering T1, T2, and T3 are each less than 2 m thick.

Relative to the North Qilian Shan segment, the river valley is broader, and each terrace is wider and less elevated above the riverbed in the Huangcheng basin segment (Figures 4, S1). T4a is the best preserved and most continuous terrace; its fill is more than 17 m thick, and the thickness of the covering aeolian loess gradually decreased from 6–10 m to around 2–3 m downstream. T3 has a narrow terrace surface and gradually disappears downstream, likely eroded by lateral incision before deposition of T2. T2 and T1 here were filled with around 5–8 m and 12–15 m thick fluvial gravels, respectively.

Terraces are sparsely preserved in the narrow Sandaowan Valley segment, and the fluvial deposits were either covered by or mixed with colluvium. Downstream, river terraces are distributed widely within the Yangxiang basin segment (Figures 4, S1). We identify the terrace sequences here as T4b, T3, T2 and T1, of which T4b, T2 and T1 are preserved continuously, while T3 is mostly absent. The thickness of the T4b fluvial deposits is 15–18 m, capped with loess of 50–80 cm thick within the Yangxiang basin and 9–14 m thick near the Dahuang Shan anticline. T3 has a narrow surface (<50 m) in this area; it has around 13 m of fluvial gravel, covered by 15–25 cm thick of loess. T2 is much wider than T3, and its tread is 10–12 m on average above the current riverbed. The T1 terrace is around 6–8 m above the riverbed and covered by 10–30 cm of loess. The loess layers covering T3-T1 have all increased their thickness toward the Dahuang Shan anticline, similar to T4b.

All four levels of terraces are well preserved on both sides of the Dahuang Shan Valley (Figures 4, S1). T4b has 11–20 m thick gravel fill, capped with 7–12 m thick loess, and its tread lies about 44 ± 4 m above the riverbed within the central Dahuang Shan. Within the center of the Dahuang Shan anticline, T3, T2, and T1 have 10–20, 8–15, and 5–10 m thick gravel fill covering the bedrock strath; their treads lie 34 ± 3, 25 ± 2, and 18 ± 2 m above riverbed, respectively.

At the piedmont of the Dahuang Shan, terraces expanded and grade into alluvial fans within the Yongchang basin. In the basin, T3 gradually merges with the T2-equivalent alluvial fan, which in turn buries the T4b fan surface underneath. The T1 terrace is absent here (Figures 4, S1). Presently the Dongda river incises into the fan deposits, forming a 9 m deep braided channel.

4.2 Dating results

We obtained a charcoal age of 30.7 ± 0.3 cal kyr BP (Field. No 93) (Figures 5, S2, Table 1) from hillslope debris within the bottom layers of T4b overlying loess at the southern end of the Yangxiang basin. In the Dahuang Shan anticline, located 5–8 km north of the previous sample site, two OSL samples were collected from the basal loess capping the T4b tread, rendering younger age results of 20.8 ± 3.6 ka (Field. No YX03) and 27.4 ± 2.5 ka (Field. No DT3-1), respectively (Figures 5, S2, Table 2). At the northern end of the Dahuang Shan, two OSL samples, one from the coarse sand layer ~30 cm below the T4b tread and another from the bottom of the T4b covering loess, render age results of 38.9 ± 4.0 ka (Field. No DT4-1) and 19.3 ± 1.9 ka (Field. No DT4-2), respectively (Figures 5, S2, Table 2).

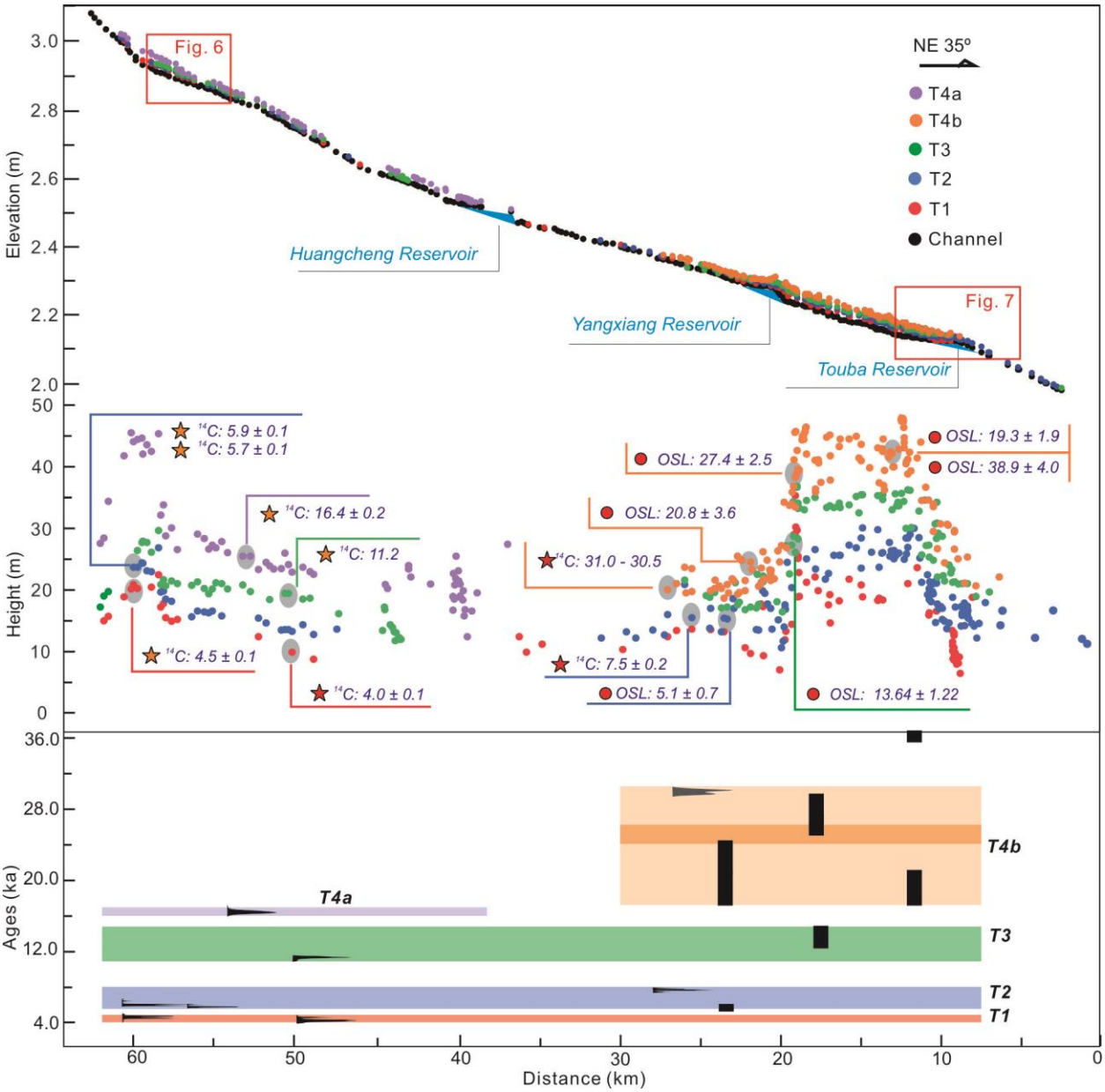

Figure 5 Top: Longitudinal profiles of the Dongda River terraces (Table S1) and riverbed (upper) and the terrace relative heights above the riverbed (lower). Each points represent the survey point of the terrace tread. The red stars, circles with the characters show the radiocarbon, and OSL dating results in this work, respectively. Orange stars show the charcoal ages results in previous studies of Xiong et al. (2017) and Lei et al. (2020). Bottom: Age model for the terrace sequences along Dongda River. Bars show 95% confidence range of OSL ages, and ^{14}C ages shown as probability density functions.

Table 1 Radiocarbon Dating Results for the Abandonment of Each Terrace Tread

Lab.No	Sample location	Terrace	Material	Field. No	^{14}C ages (BP)	Calibration age (±2σ) (kyr. BP)	Cited references
BA170047	101.64768 37.88602	T4a	Charcoal	60-61-2	13.600±50	16.4±0.2	Lei et al., 2020

BA170057	101.92680 37.98520	T4b	Charcoal	93	26440±100	30.8±0.2	
BA170053	101.75263 37.88554	T3	Charcoal	74-1	9760±35	11.2	Lei et al., 2020
HC29*	101.57629 37.84665		Charcoal	HC29	5200±30	5.9±0.1	Xiong et al.,2017
HC30*	101.57629 37.84665	T2	Charcoal	HC30	4980±30	5.7±0.1	Xiong et al.,2017
BA170060	101.94764 37.99827		Charcoal	101-102	6545±45	7.5±0.2	
BA170055	101.75256 37.88542	T1	Charcoal	74-3	3640±30	4.0±0.1 (68.2%)	
HC24*	101.57948 37.84829		Charcoal	HC24	3995±30	4.5±0.1	Xiong et al., 2017

Note: * means the results from Xiong et al. (2017) done by Beta laboratory and that from Lei et al. (2020) done by AMS 14C dating laboratory of Peking University. New carbon dating was analyzed at AMS 14C dating laboratory of Peking University. All the errors were corrected to 2σ (95.4%).

Table 2 OSL Dating Results from Loess Cover of Dongda River Terraces

Lab.No	Sample location		Field. No	Depth (m)	U (Bq/kg)	Th	Ra	K	Annual denses (Gy/ka)	Equiv. dense (Gy)	Ages(ka) (±2σ)
17- 386	101.9796 38.0982		DT4-1	1.2	28.7±1.0	38.4±1.4	390.8±21.2	28.1±6.7	3.1±0.2	120.3±8.9	38.9±4.0
17- 387	101.9796 38.0982		DT4-2	1.5	61.8±2.0	68.2±2.4	543.4±29.4	64.0±11.7	5.1±0.4	98.9±6.0	19.3±1.9
17- 388	101.9584 38.0485	T4b	DT3-1	1.7	44.2±1.4	61.4±2.2	552.5±29.8	44.5±10.8	4.5±0.3	124.2±6.6	27.4±2.5
18- 294	101.9565 38.0333		YX03	9.8	52.3±1.6	55.3±1.8	579.4±28.1	62.9±12.2	4.5±0.6	94.4±11.1	20.8±3.6
17- 389	101.9600, 38.0464	T3	DT2-2	1.4	42.4±1.4	65.8±2.4	568.7±30.7	37.7±8.3	4.6±0.3	63.2±3.3	13.6±1.2
18- 293	101.9550, 38.0270	T2	YX01	1.2	80.2±2.4	82.2±2.5	768.2±36.9	138.8±14.3	7.3±0.9	37.3±1.8	5.1±0.7

Note: Optically stimulated luminescence dating was conducted at the OSL Chronology Laboratory of the Institute of Crustal Dynamics, China Earthquake Administration. Results are reported with 2σ errors.

We obtained new ages for the younger T3 and T2 terraces. For the T3 terrace tread, we obtained one OSL age, 13.6 ± 1.2 ka (Field. No. DT2-2) from the bottom of the overlying loess from the backlimb of the Dahuang Shan (Figures 5, S2, Table 2). For the T2 terrace, at the southern end of the Yangxiang basin, one charcoal sample was collected from the covering loess ~10 cm above the tread, giving an age of 7.5 ± 0.1 cal kyr BP (Field. No. 101-102). An OSL samples from the base of the loess covering the terrace, collected at the northern end of the Yangxiang basin, gives an age of 5.1 ± 0.7 ka (Field. No. YX01) (Figures 5, S2, Table 2).

Our OSL and ^{14}C results for T4b terrace suggest a wide range of possible abandonment age (19–39 ka) (Figure 8). However, it is worth noting that the oldest sample, 39 ka (Field No. DT4-1), is from fluvial deposits (Figure S2), while the second oldest sample, 31 ka (Field No. 93), is collected from colluvial deposits (Figure S2) and the possibility of the charcoal being reworked cannot be excluded. Therefore, we suggest that both sample ages can only be treated as the upper

bound and the T4b abandonment is likely later than 31 ka ago. The remaining three other OSL dating results are all from the base of the loess cap, which indicates the lower bound of the T4b abandonment age should be around 19–27 ka (Figure 8). Previous research show that the T4b equivalent alluvial fan at the piedmont of Dahuang Shan has OSL ages of ~27 ka, ~24 ka, and ~21 ka, for samples collected from the coarse sand layers below the alluvial fan surface, and from the overlying loess 10 cm, and 50 cm above the gravel surface respectively. Considering the age sequences along the Dongda River and from the abandoned alluvial fans, we suggest the OSL age of 27.4 ± 2.5 ka is the closest approximation of the T4b abandonment age of the Dahuang Shan area (Figure 8). Within the upstream Huangcheng basin, previous research from Lei et al. (2020) reported a ^{14}C age at the loess bottom of T4a (T6 in his work) as 16.4 ± 0.2 cal kyr BP (Figures 4, 5, S3 Table 1; Field. No 60-61-2*). The disagreement in ages for T4a between the Qilian Shan-Huangcheng area (~16.4 ka) and the T4b at Yangxiang basin-Dahuang Shan -Yongchang basin area (~27.4 ka) suggests that either they represent the ages of two different terrace levels, or the abandonment of T4 was diachronous due to the growth of the Dahuang Shan anticline (Figure 8). Apart from the T4 terrace, our age results for T1- T3 terraces are in good agreement with previous studies (Xiong et al., 2017; Lei et al., 2020) along the river (Figures 4, 5, 8, Tables 1, 2). We therefore suggest that the three younger terrace levels were abandoned synchronously along the river around 11–14 ka, 6–8 ka, and ~ 4 ka, respectively.

4.3 Terrace deformation and tectonic uplift rate distribution

4.3.1 Terrace offsets and Active faults

At the mountain front of North Qilian Shan, all four terrace levels are displaced due to activity of the Minle-Damaying fault (Figures 6 and S3). A small scale (~800 m wavelength) drag fold is developed near the fault tip. Upstream of the fault trace, terrace treads of T1-T4a are 42–47, 24–29, 20–23, and 15–19 m above the riverbed. Downstream of the fault trace, the terraces treads are 25–30, 16–18, 12–14, and 10 m above the riverbed respectively. The vertical distances between the best-fit lines of each terrace within 2~4 km range both upstream and downstream of the Minle-Damaying fault suggest accumulated fault throw of 14.7 ± 0.3 m, 9.1 ± 0.2 m, 6.9 ± 0.2 m and 6.3 ± 0.2 m since the abandonment of T4a, T3, T2, and T1, respectively.

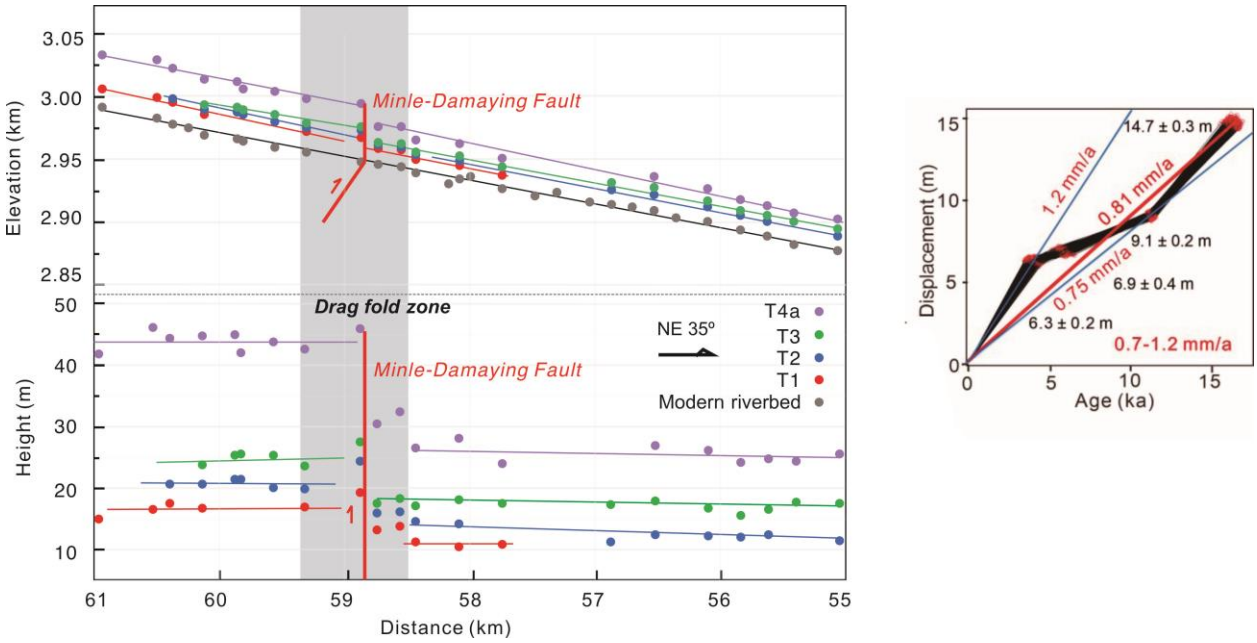

Figure 6 The river terrace tread deformation across the Minle-Damaying fault. Left: Terrace tread profiles in height above riverbed and elevation at the mountain front of North Qilian Shan. linear fits of the hangingwall and footwall. Right: tread offsets and the linear fits for the fault offset on each terrace, and the regressed slip rate for average, and range of 95% confidence.

At the mountain front of the Dahuang Shan, the displaced terrace surfaces indicate that there are three active fault strands of the Fengle fault, F1, F2, and F3 distributed across a 3.2 km wide fault zone (Figures 7 and S4). Outcrops in near Dongda river outlet suggest the dip angles are 30°±2°, 22°±2°, and 22°±2° for F1, F2, and F3, respectively (Figure S4). Downstream, within the footwall, T4b, T3 and T2 merge into a single alluvial fan, while T1 gradually lowers its height and disappears into the present channel. All three fault branches displacedT4 surface, while T1-T3 terraces show no obvious sign of offset. The vertical distances between the best-fit line of the T4 tread up-and-downstream of the fault traces indicate 9.4 ± 0.5 m, 2.3 ± 0.2 m, and 2.5 ± 0.2 m of throw for F1, F2, and F3, respectively.

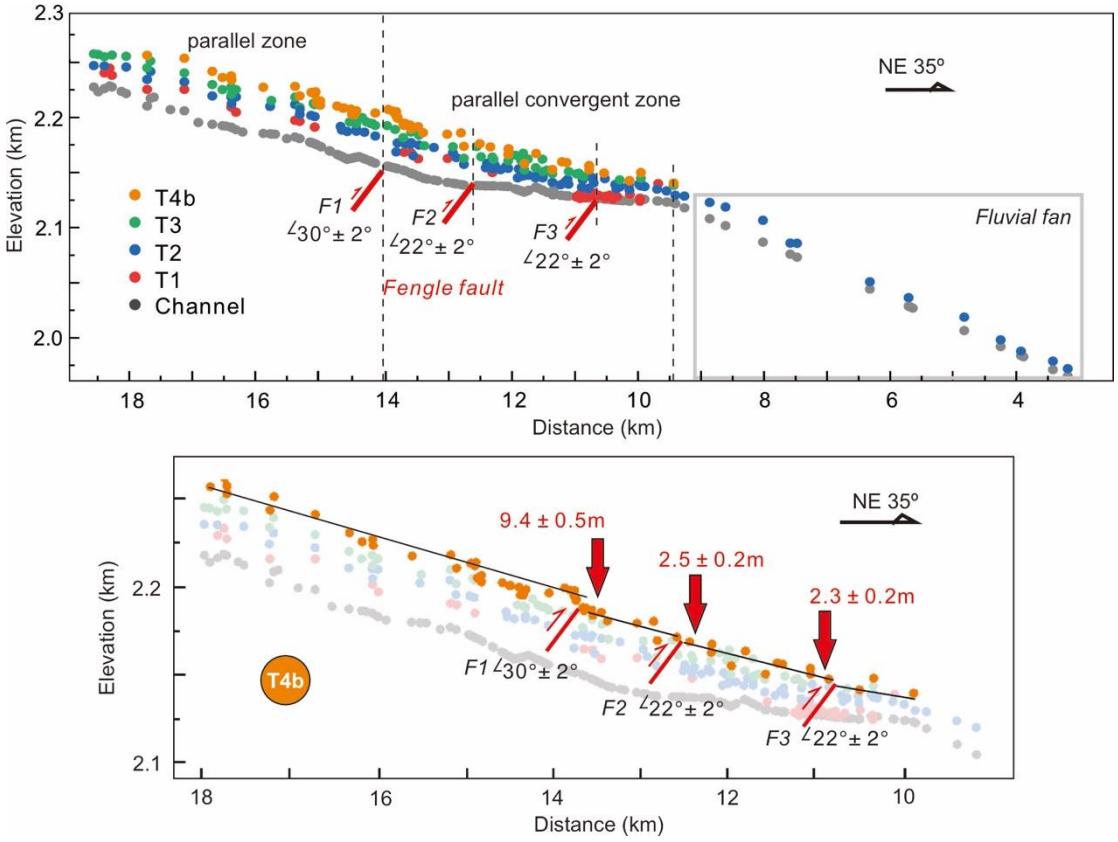

Figure 7 The river terrace deformation across the Fengle fault. Top: River terrace profiles in elevation within the Yongchang basin. Bottom: linear fits and surface offsets of T4b tread.

In between the Minle-Damaying fault and the Fengle fault, we found no obvious terrace offsets along the Dongda river. Instead, the relative heights between the four levels of terraces vary from south to north, indicating the possibility of changing uplift rate due to folding.

4.3.2 terrace deformation and active structures

Combining the fault vertical offset and the abandonment ages for each terrace tread, we estimate the vertical slip rate along the Minle-Damaying fault as 0.7–1.2 mm/a, and along Fengle fault as 0.5–0.7 mm/a. Apart from surface displacement, the vertical uplift of the region can be known from the relative heights between different terrace levels. We demonstrate this by subtracting T3 and T2 elevation from T4 terrace profile, and by subtracting the T2 elevation from T3 terrace profile; these data are then projected to a NE35° vertical plane, perpendicular to the strike of the Fengle and Minle-Damaying faults. We interpret these relative height profiles to represent the vertical uplift patterns during different periods (Figure 8), with the assumption that the original elevation of T2-T4 were similar when they were formed. This assumption can be justified by the fact that these three terraces are all fill terraces in all channel reaches, indicating they were formed under similar hydrological conditions, and therefore likely share similar original channel gradients. In addition, in the footwall of the Fengle fault within the Yongchang basin, T2-T4 merge into the same fan surface while T1 seemingly merges into the modern riverbed, indicating the base levels were the same during the formation period of T2-T4.

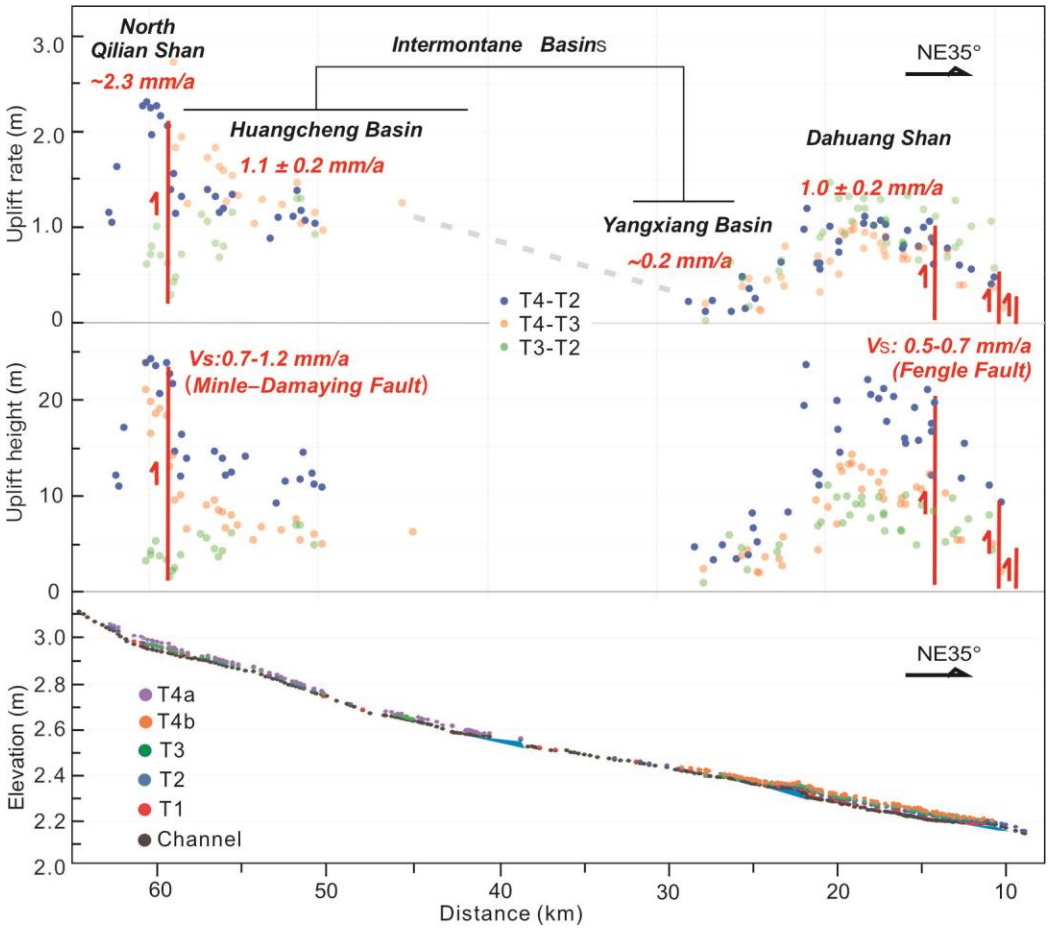

Figure 8 Bottom: the projected longitude profile of the absolute elevation for each terrace. Top: relative terrace height and uplift rate estimated from differencing elevations of T2, T3 and T4 terraces.

Dividing the vertical incision data with the duration between the abandonment of two terraces, we interpret an uplift rate profile of the region (Figure 8). The uplift rates between T2 and T3, and between T3 and T4 correlate well in Dahuang Shan region, while across the Minle-Damaying fault, the uplift rate seems to be more variable since the abandonment of T4 (Figure 7). Here, we choose the incision profile between the abandonment of T4 and T2 as the average uplift rate for further analysis and to compare between different channel reaches. Throughout the Donga River drainage, the uplift rate profile features two anticlines, a southern anticline uplifting the North Qilian Shan, and a northern anticline uplifting the Dahuang Shan, linked by a pair of intermontane basins with inhomogeneous uplift. The uplift rate quickly drops to zero north of the Fengle fault zone (Figures 8, 9). The Dahuang Shan anticline has a maximum uplift rate of 1.0 ± 0.2 mm/a at its 6.8 km long crest. The uplift rate gradually drops to ~0.2 mm/a toward south, forming a 5 km long backlimb. South of the Dahuang Shan, the uplift rate seems to be stable at ~0.2 mm/a within the 2 km wide Yangxiang basin, while the Huangcheng basin in the south has a higher uplift rate of 1.1 ± 0.2 mm/a. Lacking terrace data along the 15 km long reach between Yangxiang and Huangcheng basin makes it impossible for us to determine whether this change of uplift rate is gradual, due to faulting, or abruptly changes across an active fault. However, our field survey found no evidence of surface faulting in this area. Further south, the activity of the Minle-Damaying fault raises the total uplift rate to 2.3 ± 0.3 mm/a at the North Qilian Shan

Mountain front. Though poor preservation of terraces within the North Qilian Shan prevents us from further constraining the uplift rate pattern here, this high uplift rate appears to decrease to approximately 1.0–1.6 mm/a further into the mountains based on the few terrace survey points we collected.

5 Discussion

5.1 Regional fault structure and crustal shortening rate

Using the uplift rate profile and the kinematic fault bend fold model under the assumption that the slip rate remains constant within a fault segment, we deduce the overall geometry of the thrust system underlying the eastern North Qilian Shan. Combining the fault dip information from the previous trench work across each fault (Lei et al., 2020; Zhong et al., 2020), we estimate the slip rate along the 45° ± 10° dipping Minle-Damaying fault is 1.0–1.7 mm/a. Along the Fengle fault, a fault slip rate of 1.1–1.3 mm/a is distributed across three sub-branches dipping 30°, 22°, 22°, respectively. Assuming the slip rate remains constant at depth, the main Fengle fault underneath the Dahuang Shan anticline, where the three sub-branches merge into, should have a dip angle of 55° ± 12° for the 1.3–1.5 mm/a slip rate and the 1.0 ± 0.2 mm/a vertical uplift rate at the axil top of the fold (Figure 9). We suggest this planar fault then bends into a listric section at ~3.2 km depth, leading to southward tilting of the backlimb (Figures 9 and S5). The fault then soles into a décollement at ~7.8 km depth beneath the Yangxiang basin, which is constrained by the location of the lower axis of the backlimb of the Dahuang Shan anticline. We suggest the lowest uplift rate that we documented at the northern end of the Yangxiang basin, ~0.2 mm/a, results from slip along a gently south dipping décollement, with dip angle estimated to be 10° ± 1°.

The increase of uplift rate between Yangxiang and Huangcheng basin may be explained by two alternative models. The first model correlates this surface deformation slip on an active, blind strand of the Huangcheng-Ta'erzhuang fault, while the second model suggests this change of uplift rate is the result of increasing dip angle of the décollement. We prefer the first model for two reasons. First, for the second model, uplift rate increases from ~0.2 mm/a to 1.1 mm/a suggests the 10° ± 1° décollement may have to transfer into a steep (~65°) ramp at ~15 km depth. Considering the width of the area south of Yangxiang basin, this deep ramp would have to extend >40 km depth (Figure 9). This is well beyond the depth of seismicity (10–25 km) in the area (He et al., 2020; Deng et al., 2020). Second, previous work on the Xiying and Jinta river suggests a ~0.5 mm/a difference of incision rate across the Huangcheng-Ta'erzhuang fault trace (Pan et al., 2013a) (Figure 2b). This is similar to the uplift pattern we observed between Yangxiang and Huangcheng-Ta'erzhuang basins. Therefore, we model the Huangcheng-Ta'erzhuang fault as an active blind fault which soles into the décollement at ~15 km depth. Adopting a dip for the Huangcheng-Ta'erzhuang fault of 50°–80°, similar to that observed at Dongdingqing (Hou, 1998; Zheng et al., 2004), we infer a slip rate of 0.9–1.3 mm/a, and that the total slip rate along the 10° décollement increases to 2.3 ± 0.3 mm/a.

The high uplift rate, ~2.3 mm/a, of the North Qilian mountain front, results from the combined activity along the south dipping décollement, the Huangcheng-Ta'erzhuang fault, and the Minle-Damaying fault. The slip along the décollement and the Huangcheng-Ta'erzhuang fault leads to ~1.1 mm/a of uplift, and the slip along the Minle-Damaying fault leads to 0.7–1.2 mm/a of uplift. Further south, the uplift rate quickly drops to 1.1–1.6 mm/a, which we suggest is because this

area is only under the influence of the décollement and the Minle-Damaying fault, and effect of the Huangcheng-Ta'erzhuang fault diminishes. In this area, we predict that the Minle-Damaying fault gradually soles into the décollement at ~20 km depth, which is consistent with the results from previous geologic studies (i.e., Gaudemer et al., 1995) and InSAR inversion (Daout et al., 2016). With this model, we estimate a total slip rate of 3.0–4.3 mm/a before the décollement merges into the Haiyuan fault.

In summary, we find evidence for three active fault strands distributed across a 70 km-wide fold and thrust belt of the eastern North Qilian Shan. The northernmost strand is the Fengle fault system, which accommodates a shortening rate of 1.1–1.3 mm/a, contributing to uplifting and folding of the Dahuang Shan anticline as well as uplifting of the intermontane Yangxiang basin. The intermediate strand is a blind westward continuation of the Huangcheng-Ta'erzhuang fault, absorbing 0.9–1.3 mm/a of shortening and contributing to uplift of Huangcheng basin and part of the North Qilian Shan. The southernmost Minle-Damaying fault system slips at a rate of 1.1–1.7 mm/a, leading to 0.7–1.2 mm/a of shortening, responsible for additional uplift of the North Qilian Shan. Together, these fault systems accommodate 2.7–3.8 mm/a of total crustal shortening across a ~70 km wide frontal thrust system north of the Haiyuan fault (Figures 9 and 10), in agreement with the present-day shortening rate of ~3 mm/a measured by GPS (Wang and Shen, 2020).

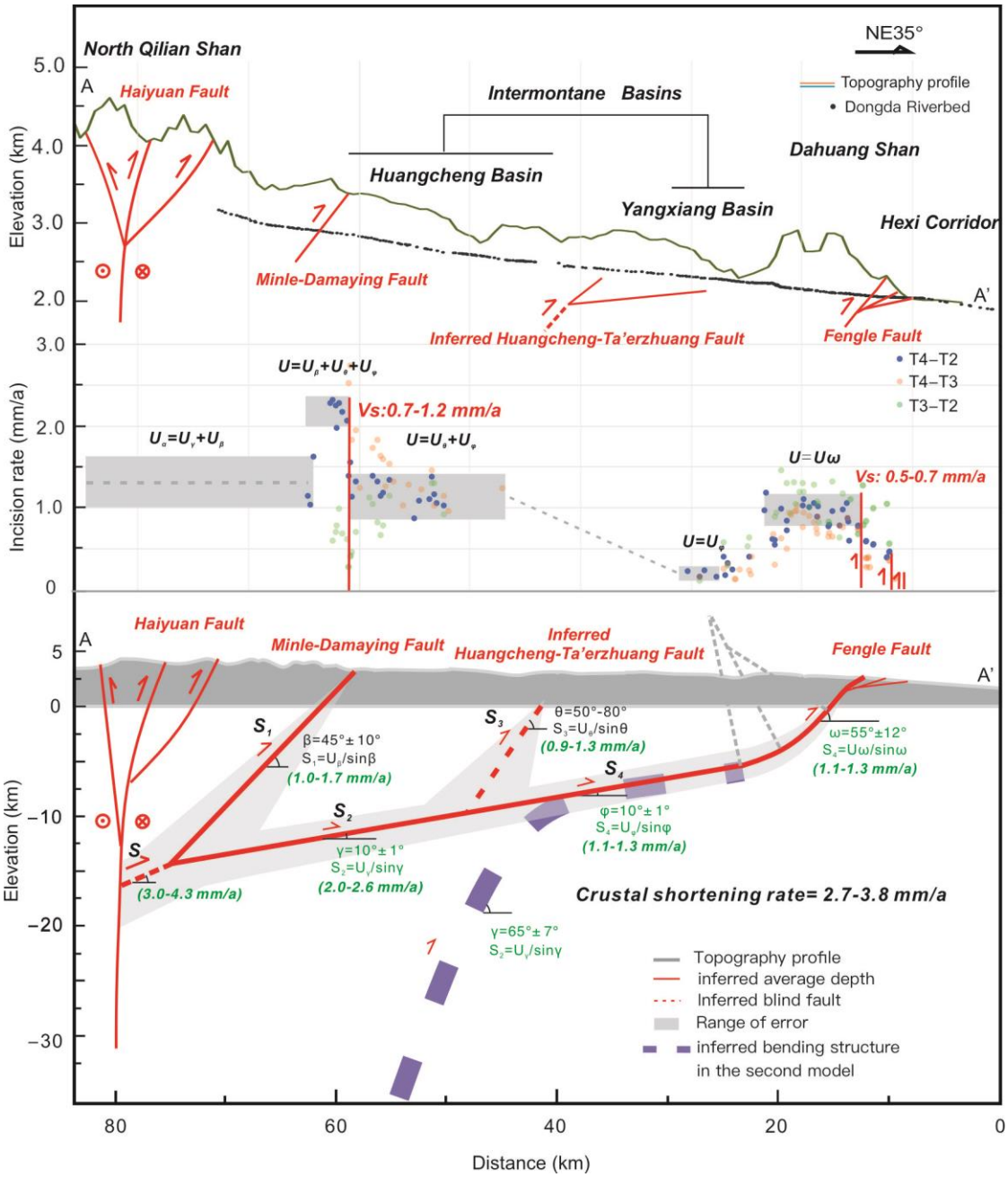

Figure 9 Top: The topography profile A-A' in Figure 2b and projected riverbed profile, Middle: The projected uplift rate profile. Bottom: Schematic block diagram showing the river terrace deformation and coupling results of underlying fault structure involve the entire seismogenic crust of the eastern Qilian Shan with respect to the Haiyuan fault. The red line within the light grey strips illustrates the average depth with errors in 95% confidence. Dashed blue line shows alternative fault geometry where steepening of décollement explains higher uplift rate of the Huangcheng basin.

5.2 Thrust propagation associated with the restraining bend of the Haiyuan fault systems

Oblique convergence across the eastern North Qilian Shan is accommodated by strike-slip on the Haiyuan fault and thrusting of the Qilian frontal and foreland fault system (Figure 9 and that in

Gaudemer et al., 1995; Hu et al., 2015). First proposed by Gaudemer et al. (1995), the growth of the foreland fold-and-thrust belt in our research area may be further enhanced by the development of a double restraining bend along the Haiyuan fault where its strike changes from east to southeast and then eastward again (Figure 1). Synthesizing our findings with previously published results from areas to the east and west shows an along-strike distinct pattern of shortening rate consistent with the restraining bend model. We find high shortening rates along the outer faults and surrounding restraining section of the Haiyuan fault, and relatively lower shortening rates along the inner faults and to the east and west of the bend. The Late-Pleistocene shortening rate along the Fengle Fault is up to 2.8 mm/a, much larger than the <1.3 mm/a shortening rate along the Huangcheng-Ta'erzhuang Fault and that of ~1.5 mm/a along the Minle-Damaying fault. At the western end of the bend, the Yonggu anticline was developed, accommodating 2.7 ± 0.6 mm/a shortening rate together with the Minle-Damaying Fault (Zhong et al., 2020). To the east, in the Dongda River area, the total shortening rate increases to 3.2 ± 0.5 mm/a (this study). Further east, by assuming that all the reverse faults sole into the same 10° décollement, we recalculated the total shortening rates along Xiying, Jinta and Zamu River as 4.5 ± 1 mm/a, 1.5 ± 0.3 mm/a, 0.5 ± 0.3 mm/a, respectively (Champagnac et al., 2010; Pan et al., 2013a; Hu et al., 2015; Ai et al., 2017). East of the restraining bend, both the foreland fold-and-thrust belt and the North Qilian Shan diminish. In contrast, the slip rate of Haiyuan fault, constrained by displaced late Pleistocene terraces, increases from 3.9 ± 0.5 mm/a south of the Tongziba river (Yuan et al., 2008) and Dongda-Xiying river region (He et al., 2000), to 6.4 ± 0.7 mm/a east of Jinta river region near the intersection with the Gulang Fault (Guo et al., 2017, 2019; Yao et al., 2019; Shao et al., 2020) (Figures 2 and 10). Further east, the Gulang Fault slips left-laterally at a rate of 1–2 mm/a (Li et al., 2019; Zhang et al., 2019), whereas the Haiyuan Fault slips at a rate of 4.4–4.8 mm/a (Liu et al., 2020) (Figures 2 and 10).

This pattern of cumulative shortening and fault slip shows that oblique convergence between the Tibetan Plateau and the Alashan Block is accommodated more by thrust faulting and folding in the restraining bend area, whereas left-lateral slip of the Haiyuan Fault and Gulang Fault accommodates most of the convergence east of the restraining bend. The eastward diminishing shortening rate across the foreland fold-and-thrust belt and the North Qilian Shan is likely a result of the changing orientation and increasing slip rate of the Haiyuan Fault and Gulang Fault. Adding up the vectors of strike-slip and shortening by thrust faulting in each area, we find the total oblique convergence rate remains constant at ~5–7 mm/a with an azimuth of 85–95° across the restraining bend (Figure 10), which is consistent with the GPS velocity data (Wang and Shen, 2020).

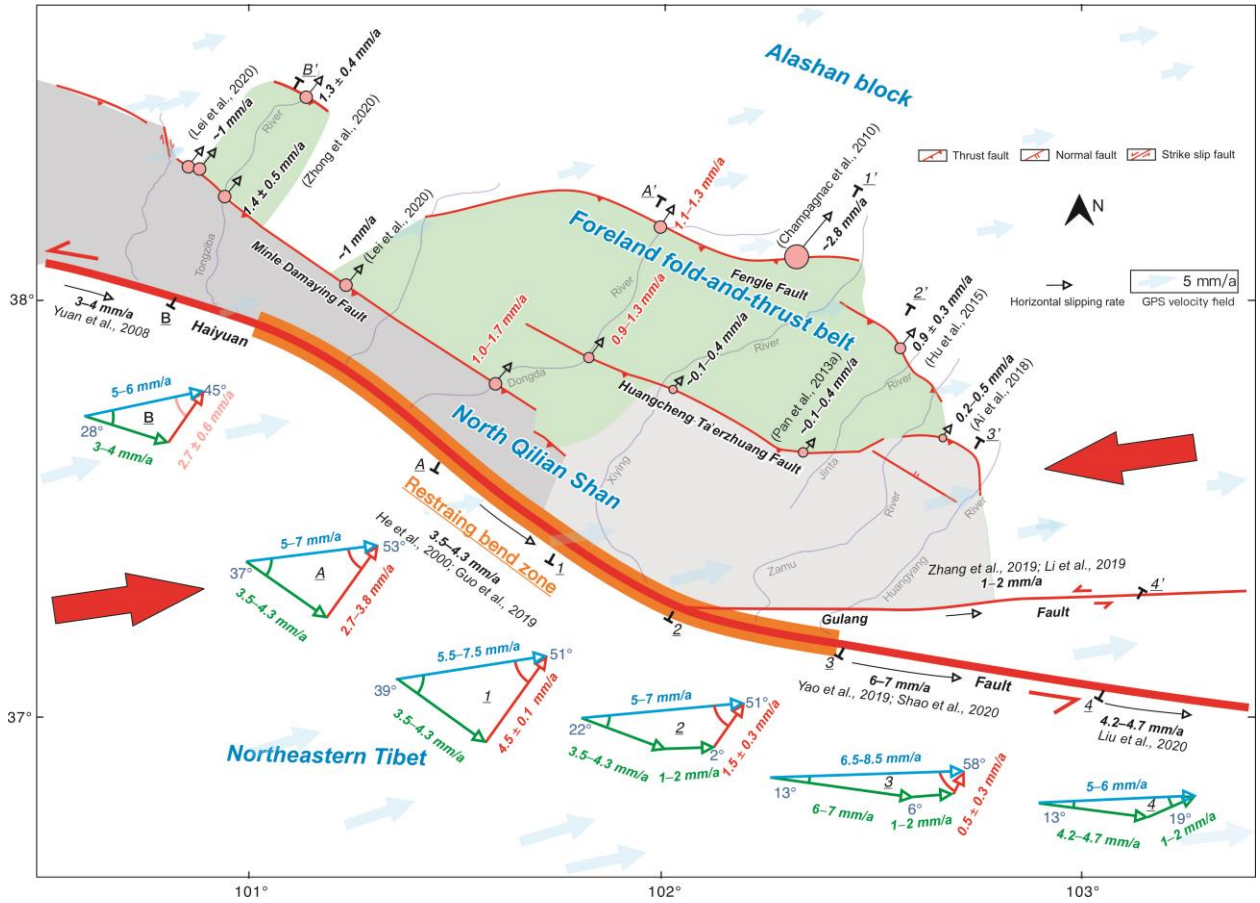

Figure 10 Mapping of the mountain front thrusts and the foreland fold-and thrust belt bounding the restraining bend of Haiyuan fault, and the crustal shortening rates accommodated by the variable strike slip and the dip-slip components within the restraining bend zone. The dark and light gray zone depicts the northern Qilian Shan, and the light green depicts the foreland fold-and-thrust belt. The blue vector represents the azimuth of relative block motion (since late Pleistocene) through a linear combination of strike slip components (green vector) and dip-slip components (red vector). The light bold blue vector represents the azimuth of relative block motion (GPS velocity) (Wang and Shen, 2020). The bold red arrows indicate the direction of the regional convergence stress.

5.3 Concentration of crustal shortening in the eastern North Qilian Shan

The regional convergence associated with the restraining bend of the Haiyuan fault explains the higher shortening rate in the eastern North Qilian Shan compared to middle and western North Qilian Shan. Previous research suggests a shortening rate is 1.8 ± 0.4 mm/a in Zhangye area (Tapponnier et al., 1990; Hu et al., 2019) (A, B in Figure 1) and 1–2 mm/a (Hetzel et al., 2019; Wang et al., 2020, 2024; C, C-C' in Figure 1) in Jiuquan area. In addition to a higher rate of shortening, the eastern Qilian Shan exhibits a more developed and much wider active frontal fault system in our research area than the western North Qilian Shan: the maximum distance between Fengle and Minle-Damaying fault is ~50 km, and the relief of the Dahuang Shan anticline reaches ~1500 m (Figure 9). In contrast, the zone of active shortening within the western North Qilian Shan is typically less than ~15 km of width (i.e., the Yumen anticline; Figure 1).

This difference indicates a larger seismic hazard in the eastern Qilian Shan foreland. Previous research has shown Gulang and Haiyuan Fault east of the restraining bend are seismically active and are the epicenters of multiple historical large earthquakes (e.g., 1920 and 1927 Ms 8.0 earthquake) (Figure 2b). The high shortening rate across the mountain front and the foreland fold-and-thrust belt related to the restraining bend suggests that the thrust belt also has high seismic risk, especially for the area around and west of Dongda-Xiying River. In fact, frequent earthquake events with magnitudes greater than Ms 6.0 have taken place in the area during the past few years, (e.g., 1986 *Ms 6.4*, 2016 *Ms*6.4 and 2022 *Mw6.7* Menyuan earthquake) (Figure 2b). In addition, the relatively high convergence rate north of the Fengle Fault and the northward propagation of the foreland fold-and-thrust belt both indicate potential risks in the foreland basin north of the Fengle Fault.

6 Conclusions

Northward propagation of the North Qilian Shan thrust system and the activity of the foreland fold-and-thrust belt are recorded by deformation of the Dongda river terraces of the eastern North Qilian Shan. Mapping and surveying of the river terraces show that two major reverse faults, the Minle-Damaying fault and Fengle fault, are active and have offset Late Pleistocene to Holocene terrace surfaces. Offset terrace treads indicate a minimum vertical slip rate of 0.5–0.7 mm/a for Fengle fault and a vertical slip rate of 0.7–1.2 mm/a for the Minle-Damaying fault. The differential incision rate between the Huangcheng basin and Yangxiang basin also suggests activity of a blind strand of the Huangcheng-Ta'erzhuang fault that accommodates ~0.9 mm/a of uplift.

The deformation of the terrace profiles indicates folding in Dahuang Shan area as a result of the activity of the underlying Fengle fault. Our modeling result suggests the underlying fault structure is likely a 55° fault ramp that soles into a 10° décollement at 7.8 km depth. Our model further suggests the 10° décollement underlies the entire fold and thrust bet of the eastern North Qilian Shan. Both the 50-80° dipping Huangcheng- Ta'erzhuang fault and the 45° dipping Minle-Damaying fault sole into this décollement at 15 km and 20 km depth, respectively. The décollement then merges into the Haiyuan fault further south. From north to south, the shortening rate is 1.1–1.3 mm/a across the Dahuang Shan area, 0.9–1.3 mm/a across the Huangcheng- Ta'erzhuang fault, and 0.7–1.2 mm/a across the Minle-Damaying fault. Together, this 70 km wide frontal fold-and-thrust system accommodates 2.7–3.8 mm/a of crustal shortening.

This crustal shortening rate along the Dongda river is one of the highest shortening rates in the North Qilian Shan and its foreland. We suggest this elevated shortening rate is related to the concentration of compressional strain adjacent to a restraining bend of the Haiyuan fault, as originally proposed by Gaudemer et al. (1995). Summing up slip rates along strike-slip faults and shortening rates across thrust faults, we find the total oblique convergence rate is a consistent 5-7 mm/yr along the restraining bend. Therefore, the eastward diminishing shortening rate of the North Qilian Shan can be explained by increased slip and more optimal orientation of both the Haiyuan fault and the Gulang fault east of the restraining bend. We further surmise that the foreland fold-and-thrust belt of the eastern North Qilian Shan has relatively high seismic hazard due to its high crustal shortening rate.

Acknowledgments

This research was supported by Natural Science Foundation of China (Grant 42030301, 41571001, U2039201, 42172233), the National Key Research and Development Program of China (Grant 2023YFC3008603) and China Scholarship Council. Thanks to PKU AMS Lab (China) and Key Laboratory of crustal dynamics (China Earthquake Administration), for supporting us with the dating work. Dr Tao Li, Hao Liang, Yuqing Zhang, and Shibao Gao is thanked for their advice on the manuscript and figures preparation. And Dr Weilin Xin, Mr Fei Liu is thanked for their field assistance.

Open Research

Figures S1-S5 and the river terrace survey data (Table S1) in the supporting information were available at (Hu et al., 2024).

References

Ai, S., Zhang, B., & Pan., C. (2017). Surface tracks and slip rate of the fault along the southern margin of the Wuwei basin in the late Quaternary (in Chinese). *Seismology and Geology*, 39(2), 408-422. Doi: 10.3969/j.issn.0253-4967.2017.02.010

Aitken, M. J. (1998). *An Introduction to Optical Dating*. Oxford: Oxford University Press.

Allen, M. B., Walters, R. J., Song, S., Saville, C., De Paola, N., Ford, J. et al. (2017). Partitioning of oblique convergence coupled to the fault locking behavior of fold-and-thrust belts: Evidence from the Qilian Shan, northeastern Tibetan Plateau. *Tectonics*, 36, 1679–1698. Doi:10.1002/2017TC004476

Amos, C. B., Burbank, D. W., Nobes, D. C., & Read, S. A. L. (2007). Geomorphic constraints on listric thrust faulting: Implications for active deformation in the Mackenzie Basin, South Island, New Zealand. *Journal of Geophysical Research: Solid Earth*, 112, B03S11. Doi:10.1029/2006JB00429

Burbank, D. W., Leland, J., Fielding, E., Anderson, R. S., Brozovic, N., Reid, M. R., & Duncan, C. (1996). Bedrock incision, rock uplift and threshold hillslopes in the northwestern Himalayas. *Nature*, 379(6565), 505–510. DOI: 10.1038/379505a0

Burbank, D. W., &Anderson, R. S. (2011). *Tectonic geomorphology (2nd edition)*. New York: Willey Blackwell. DOI:10.1002/9781444345063: 85-116

Champagnac, J. D., Yuan, D. Y., Ge, W. P., Molnar, P., &Zheng, W. J. (2010). Slip rate at the north-eastern front of the Qilian Shan, China. *Terra Nova*, 22,180-187.

Chen, Y. G., Lai, K. Y., Lee, Y. H., Suppe, J., Chen, W. S., Lin, Y. N. N., et al. (2007). Coseismic fold scarps and their kinematic behaviour in the 1999 Chi-Chi earthquake Taiwan. *Journal of Geophysical Research: Solid Earth*, 112, B03S02. Doi:10.1029/2006JB004388

Cooke, M. L., & Dair, L. C. (2011). Simulating the recent evolution of the southern big bend of the San Andreas fault, Southern California, *Journal of Geophysical Research*,116, B04405. Doi:10.1029/2010JB007835

Daout, S., Jolivet, R., Lasserre, C., Doin, M.P., Barbot, S., Tapponnier, P., et al. (2016). Along-strike variations of the partitioning of convergence across the Haiyuan fault system detected by InSAR. *Geophysical Journal International*, 205, 536-547. Doi: 10.1093/gji/ggw028

Deng, Q. D. (2007). *Mapping of Active Faults in China (1:4000000) (in Chinese)*. Beijing: Seismological Press.

Deng, Y. F., Peng, Z. G., & Liu-Zeng, J. (2020). Systematic search for repeating earthquakes along the Haiyuan Fault system in Northeastern Tibet. *Journal of Geophysical Research: Solid Earth*, 125, e2020JB019583. https://doi.org/10.1029/2020JB019583

Erslev, E. A. (1986). Basement balancing of Rocky Mountain foreland uplifts. *Geology*, 14, 259-262.

Farr, T. G., Rosen, P. A., Caro, E., Crippen, R., Duren, R., Hensley, S., & Kobrick, M., et al. (2007). The shuttle radar topography mission. *Reviews of geophysics*, *45*(2). RG2004. Doi:10.1029/2005RG000183

Gansu Bureau of Geology and Mineral Resources. (1989). *Regional Geology of Gansu Region (in Chinese with English summary)*. Beijing: Geological Publishing House.

Gao, H. S., Pan, B. T., Wu, G. J., Li, J. J., & Guan, Q. Y. (2004). Erosion surfaces in the East Qilian Mountains and uplift of the Tibetan Plateau. *Journal of Glaciology and Geocryology*, 26(5), 540-544.

Gaudemer, Y., Tapponnier, P., Meyer, B., Peltzer, G., Guo, S. M., Chen, Z. T., et al. (1995). Partitioning of crustal slip between linked, active faults in the eastern Qilian Shan, and evidence for a major seismic gap, the

'Tianzhu gap', on the western Haiyuan Fault, Gansu (China). *Geophysical Journal International*, 120, 599-645.

Guo, P., Han, Z. J., An, Y. F., Jiang, W. L., Mao, Z. B., & Feng. W. (2017). Activities of Lenglongling fault system and seismotectonics for the 2016 Ms6.4 Menyuan earthquake. *Science China Earth Sciences*, 60, 929–942. Doi: 10.1007/s11430-016-9007-2

Guo, P., Han, Z., Mao, Z., Xie, Z., Dong, S., Gao, F., & Gai, H. (2019). Paleoearthquakes and Rupture Behavior of the Lenglongling Fault: Implications for Seismic Hazards of the Northeastern Margin of the Tibetan Plateau. *Journal of Geophysical Research: Solid Earth*, 124(2), 1520-1543. https://doi.org/10.1029/2018JB016586

Guo, P., Han, Z.J., Gao, F., Zhu, C. H., & Cai, H. L. (2020). A new tectonic model for the 1927 M8.0 Gulang earthquake on the NE Tibetan Plateau. *Tectonics*, 39, e2020TC006064. https://doi.org/10.1029/2020TC006064

He, W. G., Liu, B. C., Yuan, D. Y., & Yang, M. (2000), Research on slip rates of the Lenglongling active fault zone. *Northwestern Seismological Journal*, 22(1), 90-97

He, X. H., Zhang, Y. P., Shen, X. Z., Zheng, W. J., Zhang, P. Z., & Zhang, D. L. (2020). Examination of the repeatability of two Ms6.4 Menyuan earthquakes in Qilian-Haiyuan fault zone (NE Tibetan Plateau) based on source parameters. *Physics of the Earth and Planetary Interiors*, 299, 106-408. https://doi.org/10.1016/j.pepi.2019.106408

Hetzel, R., Hampel, A., Gebbeken, P., Xu, Q., & Gold, R. D. (2019). A constant slip rate for the western Qilian Shan frontal thrust during the last 200 ka consistent with GPS-derived and geological shortening rates. *Earth and Planetary Science Letters*, 509, 100-113. https://doi.org/10.1016/j.epsl.2018.12.032

Hoke, G. D., Giambiagi, L. B., Garzione, C. N., Mahoney, J. B., & Strecker, M. R. (2014). Neogene paleoelevation of intermontane basins in a narrow, compressional mountain range, southern Central Andes of Argentina. *Earth and Planetary Science Letters*, 406, 153-164. http://dx.doi.org/10.1016/j.epsl.2014.08.032

Horton, B. K., Capaldi, T. N., Mackaman-Lofland, C., Perez, N. D., Bush, M. A., Fuentes, F., & Constenius, K. N. (2022). Broken foreland basins and the influence of subduction dynamics, tectonic inheritance, and mechanical triggers. *Earth-Science Reviews*, 104193.

Hou, K. M. (1998). the geometric segmentation and kinematics characteristics of Huangcheng-Shuangta fault zone (in Chinese). *South China Journal of Seismology*, 18(3), 28-34.

Hu, X., Wang, Y. R., Wang, W. T., Oskin, M. E., Li, Z. G., Lei, J. H., & Li, Y. L. (2024). Fault interaction and strain partitioning deduced from deformed fluvial terraces of the Eastern North Qilian foreland, NE Tibetan Plateau [Dataset]. Center for Open Science. https://osf.io/ybdg6/?view_only=66a624a31e794dbbaa5062c86887510b

Hu, X. F., Pan, B. T., Kirby, E., Gao, H. S., Hu, Z. B., Cao, B., et al. (2015). Rates and kinematics of active shortening along the eastern Qilian Shan, China, inferred from deformed fluvial terraces. *Tectonics*, 34(12), 2478-2483. Doi:10.1002/2015TC003978

Hu, X. F., Wen, Z. L., Pan, B. T., Guo, L. Y., & Cao, X. L. (2019). Constraints on deformation kinematics across the Yumu Shan, NE Tibetan Plateau, based on fluvial terraces. *Global and Planetary Change*, 182, 103023. https://doi.org/10.1016/j.gloplacha.2019.103023

Lavé, J., & Avouac, J. P. (2000). Active folding of fluvial terraces across the Siwaliks Hills, Himalayas of central Nepal. *Journal of Geophysical Research: Solid Earth*, 105(B3), 5735-5770. https://doi.org/10.1029/1999JB900292

Lei, J. H., Li, Y. L., Oskin, M. E., Wang, Y. R., Xiong, J. G., Xin, W. L., et al. (2020). Segmented Thrust Faulting: Example from the Northeastern Margin of the Tibetan Plateau. *Journal of Geophysical Research: Solid Earth*, 125(2), 0–2. https://doi.org/10.1029/2019JB018634

Lei, J. H., Li, Y. L., Ren, Z. K., Hu, X., Xiong, J. G., Liu, F., &Liu, J. R. (2021) Variable Thrust Rates of the Eastern Qilianshan Mountain Front, Northeastern Margin of the Tibet Plateau and Its Implication to the Topography of the Yongchangnan Shan. Front. Earth Sci. 9:622568. Doi: 10.3389/feart.2021.622568

Li, B., Chen, X. H., Zuza, A. V., Hu, D. G., Ding, W. C., Huang, P. H., & Xu, S. L. (2019). Cenozoic cooling history of the North Qilian Shan, northern Tibetan Plateau, and the initiation of the Haiyuan fault: Constraints from apatite- and zircon-fission track thermochronology. *Tectonophysics*, 751, 109-124. https://doi.org/10.1016/j.tecto.2018.12.005

Li, X. N., Li, C. Y., Pierce, I. K. D., Zhang, P. Z., Zheng, W. J., Dong, J. Y., et al. (2019). New slip rates for the Tianjingshan fault using optically stimulated luminescence, GPS, and paleoseismic data, NE Tibet, China. *Tectonophysics*, 755, 64-74. https://doi.org/10.1016/j.tecto.2019.02.007

Li, Y. L., & Yang, J. C. (1998). Tectonic geomorphology in the Hexi Corridor, north-west China. *Basin Research*, 10(3), 345-352. https://doi.org/10.1046/j.1365-2117.1998.00070.x

Liu, J. R, Ren, Z. K, Zhang, H. P., Li, C. Y., Zhang, Z. Q., Zheng, W. J., et al. (2022). Slip rates along the Laohushan fault and spatial variation in slip rate along the Haiyuan fault zone. *Tectonics*, 41, e2021TC006992. https://doi.org/10.1029/2021TC006992

Lu, H. H., Li, B. J., Wu, D. Y., Zhao, J. X., Zheng, X. M., Xiong, J. G., & Li, Y. L. (2019). Spatiotemporal patterns of the Late Quaternary deformation across the northern Chinese Tian Shan foreland. *Earth-Science Reviews*, 194, 19-37. https://doi.org/10.1016/j.earscirev.2019.04.026

Luo, H., & Wang, T. (2022). Strain partitioning on the western Haiyuan fault system revealed by the adjacent 2016 Mw5.9 and 2022 Mw6.7 Menyuan earthquakes. *Geophysical Research Letters*, 49, e2022GL099348. https://doi.org/10.1029/2022GL099348

McQuarrie, N., Horton, B. K., Zandt, G., Beck, S., & DeCelles, P. G. (2005). Lithospheric evolution of the Andean fold–thrust belt, Bolivia, and the origin of the central Andean plateau. *Tectonophysics*, 399(1-4), 15-37.

Meyer, B., Tapponnier, P., Bourjot, L., Métivier, F., Gaudemer, Y., Peltzer, G., et al. (1998). Crustal thickening in Gansu-Qinghai, lithospheric mantle subduction, and oblique, strike-slip controlled growth of the Tibet Plateau. *Geophysical Journal International*, 135(1), 1-47. https://doi.org/10.1046/j.1365-246X.1998.00567.x

Moulin, A., & Cowgill, E. (2023). The Mojave section of the San Andreas Fault (California), 2: Pleistocene records of near-field transpression illuminate the atypical evolution of the restraining "Big Bend". *Geochemistry, Geophysics, Geosystems*, https://doi: 10.1029/2023GC010897

Niu, P. F., Han, Z. J., Li, K. C., Lv, L. X., & Guo, P. (2023). The 2022 Mw 6.7 Menyuan earthquake on the Northeastern margin of the Tibetan Plateau, China: complex surface ruptures and large slip. *Bulletin of the Seismological Society of America*, 113(3), 976-996. https://doi.org/10.1785/0120220163

Ori, G. G., & Friend, P. F. (1984). Sedimentary basins formed and carried piggyback on active thrust sheets. *Geology*, 12(8), 475-478. https://doi.org/10.1130/0091-7613(1984)12<475:SBFACP>2.0.CO;2

Pan, B. T., Gao, H. S., Wu, G. J., Li, J. J., Li, B. Y., & Ye, Y. G. (2007). Dating of erosion surface and terraces in the eastern Qilian Shan, northwest China. *Earth Surface Processes and Landforms*, 32, 143-154. Doi: 10.1002/esp.1390

Pan, B. T., Hu, X. F., Gao, H. S., Hu, Z. B., Cao, B., Geng, H. P., & Li, Q. Y. (2013a). Late Quaternary River incision rates and rock uplift pattern of the eastern Qilian Shan Mountain, China. *Geomorphology*, 184, 84-97. http://dx.doi.org/10.1016/j.geomorph.2012.11.020

Pan, B. T., Li, Q. Y., Hu, X. F., Geng, H. P., Liu, Z. B., Jiang, S. F., Yuan, W. M. (2013b). Cretaceous and Cenozoic cooling history of the eastern Qilian Shan, north-eastern margin of the Tibetan Plateau: Evidence from apatite fission-track analysis. *Terra Nova*, 25(6), 431-438. https://doi.org/10.1111/ter.12052

Ramsey, C. B. (2009). Bayesian analysis of radiocarbon dates. *Radiocarbon*, 51(1), 337–360. Doi: 10.2458/azu_js_rc.51.3494

Reimer, P. J., Austin, W. E. N., Bard, E., Bayliss, A., Blackwell, P. G., Ramsey, C. B., et al. (2020). The IntCal20 Northern Hemisphere radiocarbon age calibrate curve (0-55 cal kBP). *Radiocarbon*, 62(4), 725-757. https://doi.org/10.1017/RDC.2020.41

Shao, Y. X., Liu-Zeng, J., Woerd, J. V. D., Klinger, Y., Oskin, M. E., Zhang, J. Y., et al. (2020). Late Pleistocene slip rate of the central Haiyuan fault constrained from optically stimulated luminescence, ^{14}C, and cosmogenic isotope dating and high-resolution topography. *Bulletin of the Geological Society of America*, 133(7-8), 1347-1346. https://doi.org/10.1130/B35571.1

Siks, B. C., & Horton, B. K. (2011). Growth and fragmentation of the Andean foreland basin during eastward advance of fold-thrust deformation, Puna plateau and Eastern Cordillera, northern Argentina. *Tectonics*, 30, TC6017. Doi:10.1029/2011TC002944

Sun, C., Li, Z. G., Zuza, A. V., Zheng, W. J., Jia, d., He, Z. Y., et al. (2022). Controls of mantle subduction on crustal-scale architecture of intraplate orogens, insights from sandbox modeling. *Earth and Planetary Science Letters*, 584, 117476. https://doi.org/10.1016/j.epsl.2022.117476

Suppe, S. (1983). Geometry and kinematics of fault-bend folding. *American Journal of Science*, 283(7), 684-721. https://doi.org/10.2475/ajs.283.7.684

Talma, A. S., & Vogel, J C. (1993). A simplified approach to calibrating 14C dates. *Radiocarbon*, 35(2), 317-322.

Tapponnier, P., Meyer, B., Avouac, J. P., Peltzer, G., Gaudemer, Y., Guo, S. M., et al. (1990). Active thrusting and folding in the Qilian Shan, and decoupling between upper crust and mantle in northeastern Tibet. *Earth and Planetary Science Letters*, 97, 382-403. https://doi.org/10.1016/0012-821X(90)90053-Z

Tapponnier, P., Xu, Z. Q., Roger, F., Meyer, B., Arnaud, N., Wittlinger, G., & Yang, J. S. (2001). Oblique stepwise rise and growth of the Tibet plateau. *Science*, 294(5547), 1671-1677. Doi: 10.1126/science.105978

Thompson, S. C., Weldon, R. J., Rubin, C. M., Abdrakhmatov, K., Molnar, P., & Berger, G. W. (2002). Late Quaternary slip rates across the central Tien Shan, Kyrgyzstan, central Asia. *Journal of Geophysical Research: Solid Earth*, 107(B9), ETG 7-1-ETG 7-32. Doi:10.1029/2001JB000596 2203

Vries, P. H. D., & Barendsen, G. W. (1954). Measurements of age by the carbon-14 technique. *Nature*, 174, 1138-1141.

Wang, M., & Shen, Z. K. (2020). Present-day crustal deformation of continental China derived from GPS and its tectonic implications. *Journal of Geophysical Research: Solid Earth*, 125(2), e2019jb018774. https://doi.org/10.1029/2019JB018774

Wang, W. T., Zheng, D. W., Li, C. P., Wang, Y., Zhang, Z. Q., Pang, J. Z., et al. (2020). Cenozoic exhumation of the Qilian Shan in the northeastern Tibetan Plateau: Evidence from low-temperature thermochronology. *Tectonics*, 39(4), e2019TC005705. https://doi.org/10.1029/2019TC005705

Wang, Y. R., Oskin, M. E., Zhang, H. P., Li, Y. L., Hu, X., & Lei, J. H. (2020). Deducing Crustal-Scale Reverse-Fault Geometry and Slip Distribution from Folded River Terraces, Qilian Shan, China. *Tectonics*, 39(1), e2019TC005901. https://doi.org/10.1029/2019TC005901

Wang, Y. R, Oskin, M. E., Li, Y. L, Hu, X., Lei, J. H, Liu, F. (2024). Crustal-scale duplex development during accretion of the Jiuxi foreland basin, North Qilian Shan. *Tectonics*, 43, e2023TC008160. https://doi.org/10.1029/2023TC008160

Xiong, J. G., Li, Y. L., Zhong, Y. Z., Lu, H. H., Lei, J. H., Xin, W. L., et al. (2017). Latest Pleistocene to Holocene Thrusting Recorded by a Flight of Strath Terraces in the Eastern Qilian Shan, NE Tibetan Plateau. *Tectonics*, 36(12), 2973-2986. https://doi.org/10.1002/2017TC004648

Yao, W., Liu-Zeng, J., Oskin, M. E., Wang, W., Li, Z., Prush, V., et al. (2019). Reevaluation of the Late Pleistocene slip rate of the Haiyuan fault near Songshan, Gansu province, China. *Journal of Geophysical Research: Solid Earth*, 124, 5217–5240. https://doi.org/ 10.1029/2018JB016907

Yang, J. C., & Li, Y. L. (2017). *Principles of Geomorphology (4th edition, in Chinese)*. Beijing: Peking University Press.

Yonkee, W. A., Eleogram, B., Wells, M. L., Stockli, D. F., Kelley, S., & Barber, D. E. (2019). Fault Slip and Exhumation History of the Willard Thrust Sheet, Sevier Fold-Thrust Belt, Utah: Relations to Wedge Propagation, Hinterland Uplift, and Foreland Basin Sedimentation. *Tectonics*, 38, 2850–2893. https://doi.org/10.1029/2018TC005444

Yuan, D., Zhang, P., Ge, W., Liu, X., Zhang, H., & Liang, M. (2008). Late Quaternary strike-slip features along the western segment of Haiyuan-Qilianshan fault, NE Tibetan Plateau. In *AGU Fall Meeting Abstracts* (Vol. 2008, pp. T33B-2057).

Zhang, Y. P., Zheng, W. J., Zhang, D. L., Zhang, P. Z., Yuan, D. Y., Tian, Q. Y., et al. (2019). Late Pleistocene left-lateral slip rates of the Gulang Fault and its tectonic implications in eastern Qilian Shan (NE Tibetan Plateau), China. *Tectonophysics*, 756, 97-111. https://doi.org/10.1016/j.tecto.2019.02.013

Zhang, Y. Q., Chen, H. L., Shi, X. H., Almeida, R., Walker, R., Lin, X. B., et al. (2023). Reconciling patterns of long-term topographic growth with coseismic uplift by synchronous duplex thrusting. *Nature Communications*, 14, 8073. https://doi.org/10.1038/s41467-023-43994-6

Zheng, W. J., Yuan, D. Y., & He, W. G. (2004). Preliminary study of the seismicity of palaeo-earthquakes on Dongqingding segment of Huangcheng-Shuangta fault (in Chinese). *Journal of seismological research*, 27(1), 66-73.

Zheng, W. J., Zhang, P. Z., He, W. G., Yuan, D. Y., Shao, Y. X., Zheng, D. W., et al. (2013). Transformation of displacement between strike-slip and crustal shortening in the northern margin of the Tibetan Plateau: Evidence from decadal GPS measurements and late Quaternary slip rates on faults. *Tectonophysics*, 584, 267-280. https://doi:10.1016/j.tecto.2012.01.006

Zhong, Y. Z., Xiong, J. G., Li, Y. L., Zheng, W. J., Zhang, P. Z., Lu, H. H., et al. (2020). Constraining Late Quaternary Crustal Shortening in the Eastern Qilian Shan from Deformed River Terraces. *Journal of Geophysical Research: Solid Earth*, 125, e2020JB020631. https://doi.org/ 10.1029/2020JB020631

Zuza, A. V., Cheng, X. G., & Yin, A. (2016). Testing models of Tibetan plateau formation with Cenozoic shortening estimates across the Qilian Shan-Nan Shan thrust belts. *Geosphere*, 12(2), 501-532. Doi:10.1130/GES01254.1.

Zuza, A. V., Wu, C., Reith, R. C., Yin, A., Li, J. H., Zhang, J. J., et al. (2018). Tectonic evolution of the Qilian Shan: An early Paleozoic orogen reactivated in the Cenozoic. *Bulletin of the Geological Society of America*, 130(5/6), 881-925. https://doi.org/10.1130/B31721.1

Figure 1.

E97°
E100°
E103°
N38°
b
Altyn Tagh Fault
Alashan
N
5000
3000
1500
North
Hexi
C'
C
B
A
Qilian
B'
Corridor
Fig. 2
A'
Haiyuan Fault
Shan
Qaidam Basin
Xining Basin
Fig. b
North
Qilian Shan
Tibetan Plateau
a
Thrust fault
Left lateral fault
Altyn Tagh Fault
Northern Qilian Shan Fault systems
Haiyuan Fault

Figure 2.

a

E101.50°

E102.00°

E102.50°

N38.00°

N37.50°

Fengle

Yongchang

Hexi

Wuwei

Corridor

Fig. 7

A'

Lei et al., 2022
0.5–0.7 mm/a

DEM

4500 (m)

3000

1500

N

DHSA

Zhong et al., 2020
0.5-1.0 mm/a

Foreland

Champagnac et al., 2010
2.8 ± 1.3 mm/a

Minle-Damaying

Fig. 6

Dongda

river

Fold-and-thrust

Fault

Huangcheng

Belt

Ai et al., 2018
0.5–0.7 mm/a

Xiying

river

Lei et al., 2020
1.0 mm/a

1986 Ms 6.4

JTA

North

Fault

river

Ta'erzhuang

1927 Ms 8.0

Zheng et al., 2004
Ai et al., 2018
0.5 mm/a

2022 Ms 6.7
2016 Ms 6.4

2011 Ms 4.1

2014 Ms 4.5

Fault

Lenglongling

A

Haiyuan

Qilian

Shan

DQDA

Gulang

Zamu

river

Huangyang

river

3.9 ± 0.4 mm/a
He et al., 2000

1.1-2.5 mm/a
Li et al., 2019;Zhang et al., 2019

river

Menyuan

Fault

Gulang

Fault

6.4- 6.6 mm/a
Guo et al., 2019

6.4 ± 0.7 mm/a
Shao et al., 2021

5.0 - 8.9 mm/a
Shao et al., 2021

4.2-4.8 mm/a
Liu et al., 2022

Gulang

Thrust fault

Normal fault

Strike slip fault

b

E101.50°

E102.00°

E102.50°

N38.00°

N37.50°

Yongchang

Wuwei

Hexi

Corridor

Fold-and-thrust

Foreland

Belt

2

Pan et al., 2003;
Li et al., 2019
LTT: 15~10 Ma

Wang et al., 2020
LTT: 15~10 Ma, ~5Ma

3

Pan et al., 2007
ESR:1.3-1.4 Ma

3

North

Qilian

Shan

Gulang

Gao et al., 2004
Magnetic: 1.4 Ma

4

Menyuan

ϵ Cambrian

r_3 Granite

O Ordovician

S Silurian

D Devonian

C Carboniferous

P Permian

T Triassic

J Jurassic

K Cretaceous

N Neogene

Q Quaternary

H Holocene

Figure 3.

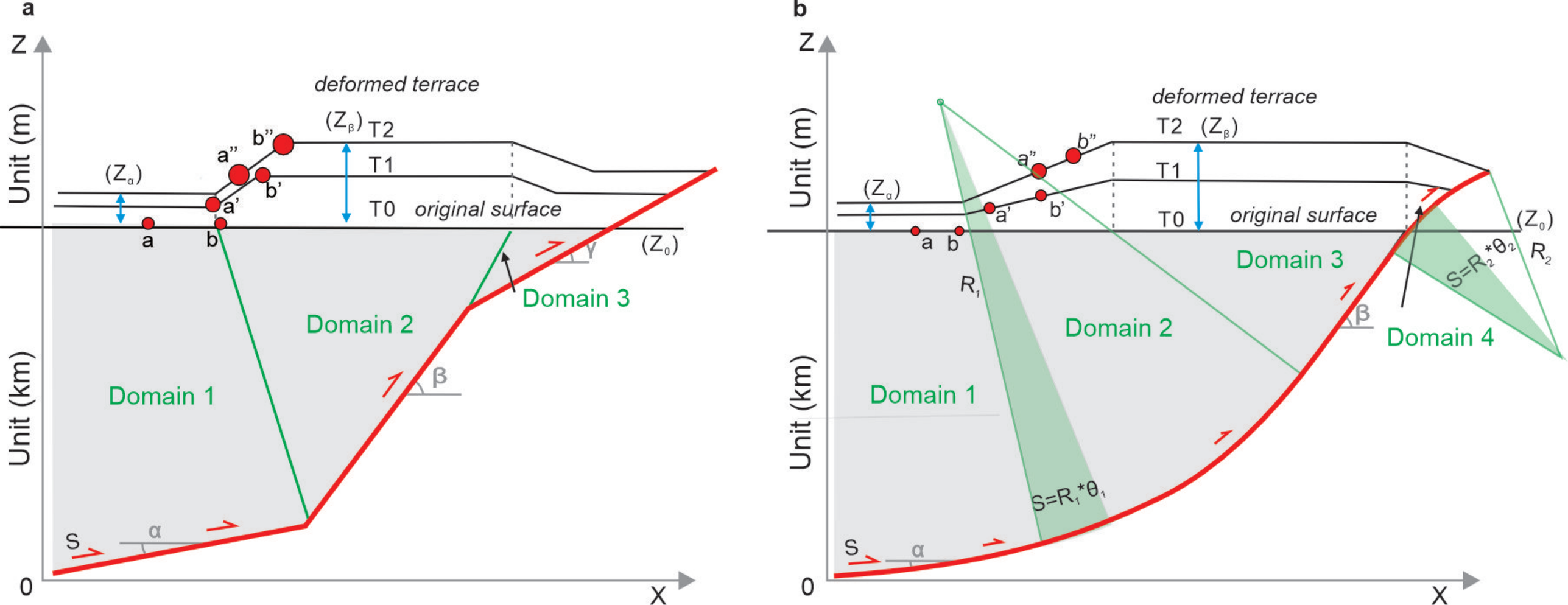
a
Z
Unit (m)
deformed terrace
(Z_β) T2
T1
T0
original surface
(Z_α)
(Z_0)
a
b
a'
b'
a''
b''
Domain 1
Domain 2
Domain 3
β
γ
α
S
Unit (km)
0
X
b
Z
Unit (m)
deformed terrace
T2 (Z_β)
T1
T0
original surface
(Z_α)
(Z_0)
a
b
a'
b'
a''
b''
R_1
R_2
$S=R_1*\theta_1$
$S=R_2*\theta_2$
Domain 1
Domain 2
Domain 3
Domain 4
β
α
S
Unit (km)
0
X

Figure 4.

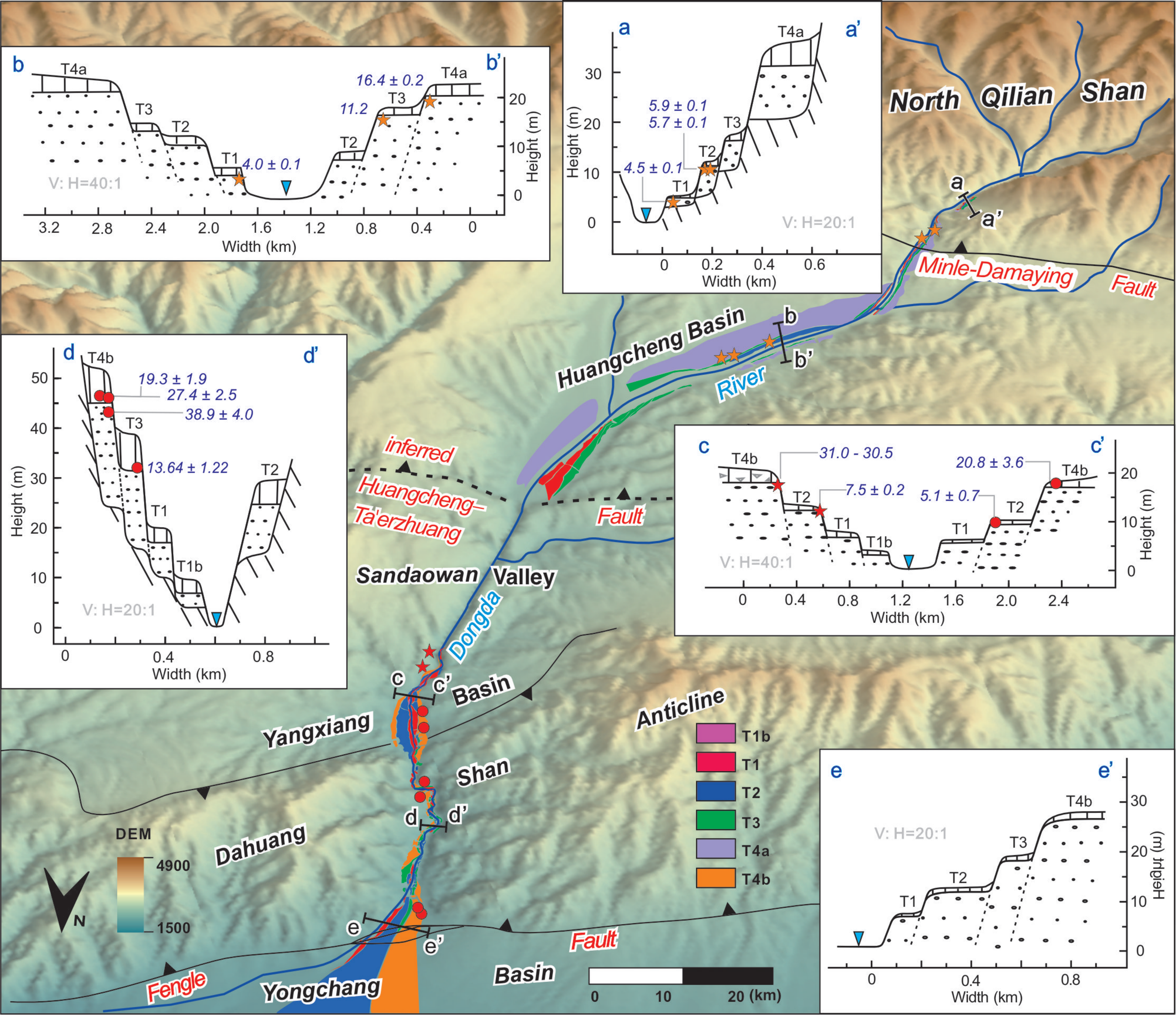
a
a'
T4a
30
20
10
0
Height (m)
5.9 ± 0.1
5.7 ± 0.1
4.5 ± 0.1
T3
T2
T1
V: H=20:1
0
0.2
0.4
0.6
Width (km)
b
b'
T4a
16.4 ± 0.2
11.2
T3
T2
T1
4.0 ± 0.1
V: H=40:1
20
10
0
Height (m)
3.2
2.8
2.4
2.0
1.6
1.2
0.8
0.4
0
Width (km)
North
Qilian
Shan
Minle-Damaying
Fault
Huangcheng Basin
River
d
d'
T4b
19.3 ± 1.9
27.4 ± 2.5
38.9 ± 4.0
T3
13.64 ± 1.22
T2
T1
T1b
V: H=20:1
50
40
30
20
10
0
Height (m)
0
0.4
0.8
Width (km)
inferred
Huangcheng–
Ta'erzhuang
Fault
Sandaowan
Valley
Dongda
Basin
c
c'
Yangxiang
Shan
Anticline
d
d'
Dahuang
DEM
4900
1500
N
e
e'
Fengle
Yongchang
Fault
Basin
T1b
T1
T2
T3
T4a
T4b
0
10
20 (km)
c
c'
T4b
31.0 - 30.5
7.5 ± 0.2
T2
T1
T1b
20.8 ± 3.6
5.1 ± 0.7
T4b
T2
T1
V: H=40:1
20
10
0
Height (m)
0
0.4
0.8
1.2
1.6
2.0
2.4
Width (km)
e
e'
T4b
V: H=20:1
T3
T2
T1
30
20
10
0
Height (m)
0
0.4
0.8
Width (km)

Figure 5.

Fig. 6

Fig. 7

T4a
T4b
T3
T2
T1
Channel

Huangcheng Reservoir

Yangxiang Reservoir

Touba Reservoir

^{14}C: 5.9 ± 0.1
^{14}C: 5.7 ± 0.1
^{14}C: 16.4 ± 0.2
^{14}C: 11.2
^{14}C: 4.5 ± 0.1
^{14}C: 4.0 ± 0.1
^{14}C: 31.0 - 30.5
^{14}C: 7.5 ± 0.2
OSL: 27.4 ± 2.5
OSL: 20.8 ± 3.6
OSL: 5.1 ± 0.7
OSL: 19.3 ± 1.9
OSL: 38.9 ± 4.0
OSL: 13.64 ± 1.22

Elevation (m)
3.0
2.8
2.6
2.4
2.2
2.0
50

Height (m)
40
30
20
10
0

60
50
40
30
20
10
0

Distance (km)

Figure 6.

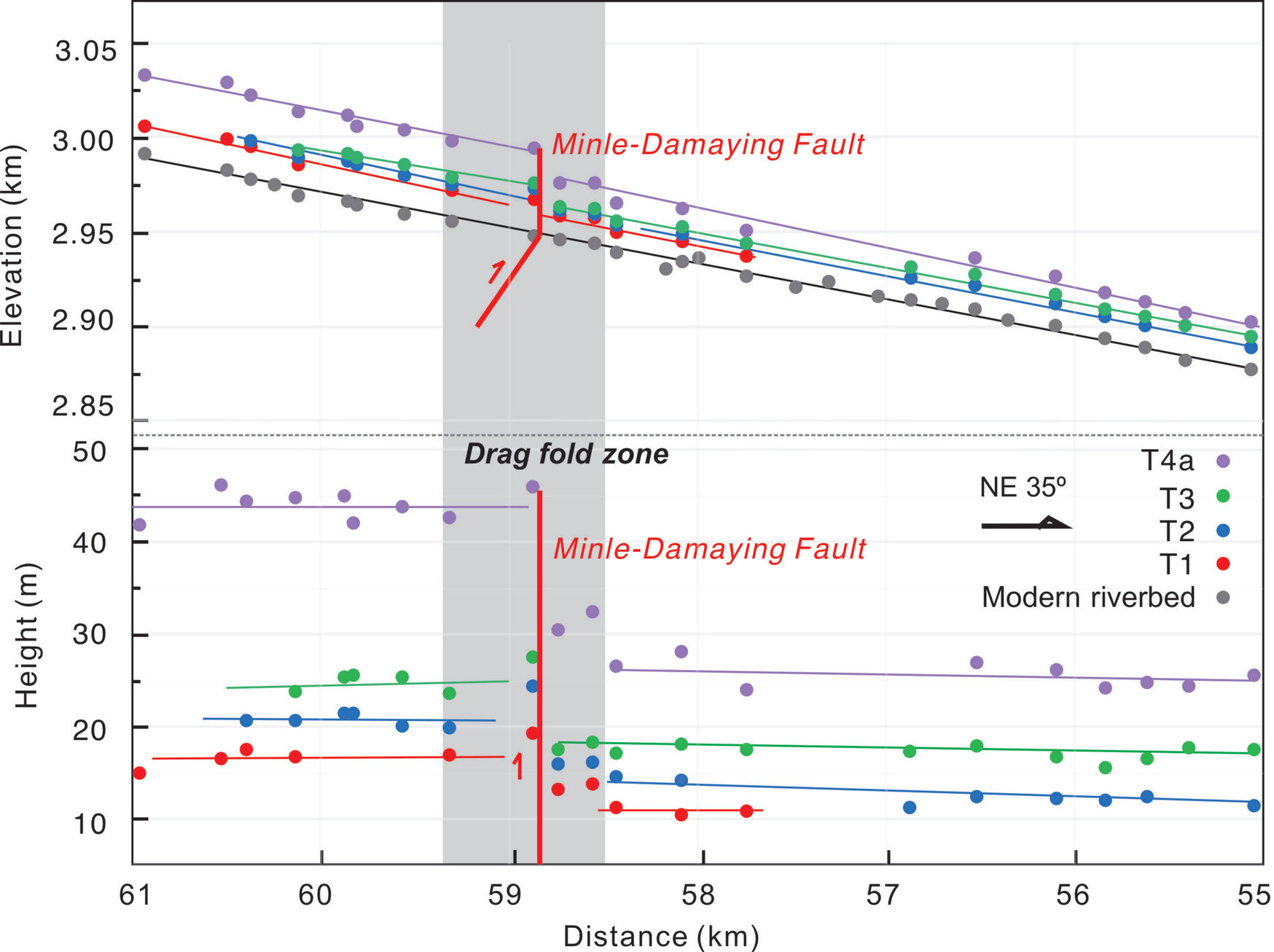
Elevation (km)
3.05
3.00
2.95
2.90
2.85
Minle-Damaying Fault
1
Drag fold zone
Height (m)
50
40
30
20
10
Minle-Damaying Fault
1
NE 35°
T4a
T3
T2
T1
Modern riverbed
61
60
59
58
57
56
55
Distance (km)

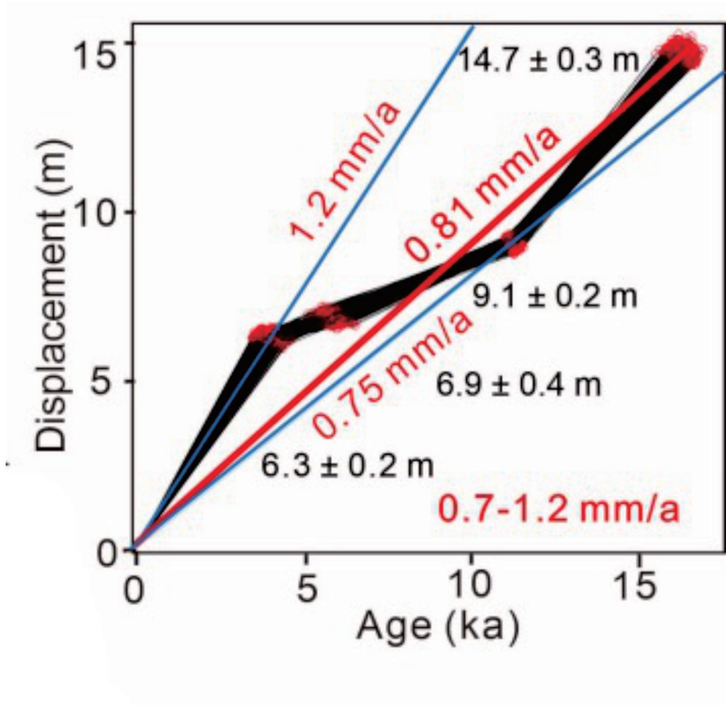
Displacement (m)
15
10
5
0
14.7 ± 0.3 m
1.2 mm/a
0.81 mm/a
9.1 ± 0.2 m
0.75 mm/a
6.9 ± 0.4 m
6.3 ± 0.2 m
0.7-1.2 mm/a
0
5
10
15
Age (ka)

Figure 7.

parallel zone

parallel convergent zone

NE 35°

T4b
T3
T2
T1
Channel

F1 ∠30°± 2°

F2 ∠22°± 2°

F3 ∠22°± 2°

Fengle fault

Fluvial fan

Elevation (km)

2.3
2.2
2.1
2.0

18
16
14
12
10
8
6
4

Distance (km)

NE 35°

9.4 ± 0.5m

2.5 ± 0.2m

2.3 ± 0.2m

F1 ∠30°± 2°

F2 ∠22°± 2°

F3 ∠22°± 2°

T4b

Elevation (km)

2.2
2.1

18
16
14
12
10

Distance (km)

Figure 8.

North Qilian Shan

~2.3 mm/a

Intermontane Basins

NE35°

Huangcheng Basin

1.1 ± 0.2 mm/a

Yangxiang Basin

~0.2 mm/a

Dahuang Shan

1.0 ± 0.2 mm/a

Uplift rate (m)

3.0

2.0

1.0

0

T4-T2

T4-T3

T3-T2

Vs:0.7-1.2 mm/a

(Minle–Damaying Fault)

Vs: 0.5-0.7 mm/a

(Fengle Fault)

Uplift height (m)

20

10

0

NE35°

Elevation (m)

3.0

2.8

2.6

2.4

2.2

2.0

T4a

T4b

T3

T2

T1

Channel

Figure 9.

NE35°

Topography profile

Dongda Riverbed

North Qilian Shan

A

Haiyuan Fault

Intermontane Basins

Huangcheng Basin

Yangxiang Basin

Dahuang Shan

Hexi Corridor

A'

Minle-Damaying Fault

Inferred Huangcheng-Ta'erzhuang Fault

Fengle Fault

T4–T2

T4–T3

T3–T2

$U=U_\beta+U_\theta+U_\varphi$

Vs:0.7-1.2 mm/a

$U_\alpha=U_\gamma+U_\beta$

$U=U_\theta+U_\varphi$

$U=U\omega$

Vs: 0.5-0.7 mm/a

$U=U_\varphi$

Incision rate (mm/a)

Elevation (km)

Haiyuan Fault

Minle-Damaying Fault

Inferred Huangcheng-Ta'erzhuang Fault

Fengle Fault

S_1

β=45°± 10°

$S_1=U_\beta/\sin\beta$

(1.0-1.7 mm/a)

S_3

θ=50°-80°

$S_3=U_\theta/\sin\theta$

(0.9-1.3 mm/a)

S_4

ω=55°±12°

$S_4=U\omega/\sin\omega$

(1.1-1.3 mm/a)

S_2

γ=10°± 1°

$S_2=U_\gamma/\sin\gamma$

(2.0-2.6 mm/a)

S

(3.0-4.3 mm/a)

φ=10°± 1°

$S_4=U_\varphi/\sin\varphi$

(1.1-1.3 mm/a)

γ=65°± 7°

$S_2=U_\gamma/\sin\gamma$

Crustal shortening rate= 2.7-3.8 mm/a

Topography profile

inferred average depth

Inferred blind fault

Range of error

inferred bending structure in the second model

Distance (km)

Figure 10.

Alashan block

Foreland fold-and-thrust belt

North Qilian Shan

Restraining bend zone

Northeastern Tibet

Thrust fault
Normal fault
Strike slip fault

N

Horizontal slipping rate

5 mm/a
GPS velocity field

Minle-Damaying Fault
~1 mm/a (Lei et al., 2020)
1.4 ± 0.5 mm/a (Zhong et al., 2020)
1.3 ± 0.4 mm/a
~1 mm/a (Lei et al., 2020)
1.0–1.7 mm/a
0.9–1.3 mm/a
~0.1–0.4 mm/a
Huangcheng-Ta'erzhuang Fault
~0.1–0.4 mm/a (Pan et al., 2013a)
1.1–1.3 mm/a
Fengle Fault
~2.8 mm/a (Champagnac et al., 2010)
0.9 ± 0.3 mm/a (Hu et al., 2015)
0.2–0.5 mm/a (Ai et al., 2018)
Haiyuan
3–4 mm/a Yuan et al., 2008
3.5–4.3 mm/a He et al., 2000; Guo et al., 2019
6–7 mm/a Yao et al., 2019; Shao et al., 2020
1–2 mm/a Zhang et al., 2019; Li et al., 2019
Gulang Fault
4.2–4.7 mm/a Liu et al., 2020

Tongziba
Dongda
River
Xiying
Jinta
Zamu
Huangyang

B: 5–6 mm/a, 45°, 28°, 3–4 mm/a, 2.7 ± 0.6 mm/a
A: 5–7 mm/a, 53°, 37°, 3.5–4.3 mm/a, 2.7–3.8 mm/a
1: 5.5–7.5 mm/a, 51°, 39°, 3.5–4.3 mm/a, 4.5 ± 0.1 mm/a
2: 5–7 mm/a, 51°, 22°, 3.5–4.3 mm/a, 1–2 mm/a, 2°, 1.5 ± 0.3 mm/a
3: 6.5-8.5 mm/a, 58°, 13°, 6–7 mm/a, 6°, 1–2 mm/a, 0.5 ± 0.3 mm/a
4: 5–6 mm/a, 13°, 4.2–4.7 mm/a, 19°, 1–2 mm/a

38°
37°
101°
102°
103°